ELSEVIER

CrossMark

Nano-mineralogy and -geochemistry of high-grade diasporic karst-type bauxite from Parnassos-Ghiona mines, Greece

Platon N. Gamaletsos [a,b,*], Athanasios Godelitsas [b], Takeshi Kasama [a], Nathan S. Church [c], Alexios P. Douvalis [d], Jörg Göttlicher [e], Ralph Steininger [e], Alexey Boubnov [f], Yiannis Pontikes [g], Evangelos Tzamos [h], Thomas Bakas [d], Anestis Filippidis [h]

[a] Center for Electron Nanoscopy, Technical University of Denmark, 2800 Kongens Lyngby, Denmark
[b] Department of Geology and Geoenvironment, National and Kapodistrian University of Athens, Zografou Campus, 15784 Athens, Greece
[c] Department of Geology & Mineral Engineering, Norwegian University of Science & Technology, 7491 Trondheim, Norway
[d] Department of Physics, University of Ioannina, 45110 Ioannina, Greece
[e] ANKA Synchrotron Radiation Facility, Karlsruhe Institute of Technology, Hermann-von-Helmholtz-Platz 1, 76344 Eggenstein-Leopoldshafen, Germany
[f] Karlsruhe Institute of Technology, Institute for Chemical Technology and Polymer Chemistry, Kaiserstrasse 12, 76131 Karlsruhe, Germany
[g] KU Leuven, Department of Materials Engineering, Kasteelpark Arenberg 44, 3001 Leuven, Belgium
[h] Department of Geology, Aristotle University of Thessaloniki, 54124 Thessaloniki, Greece

ARTICLE INFO

ABSTRACT

In the present work, a combination of various techniques is utilized for the study of nano-mineralogy and -geochemistry of high-grade karst-type bauxite (Al-rich and Fe-depleted samples; Al_2O_3 ca. 80 wt.%) from the Parnassos-Ghiona mines located in Greece. Initial characterization using PXRD and electron microscopy in micro-scale and mesoscale (SEM-EDS including STEM mode), proved the presence of "Fe-Cr-Ti-containing diaspore", anatase and minor rutile. The study by means of ^{57}Fe Mössbauer spectroscopy, in correlation with magnetic susceptibility measurements and, complemented, with Synchrotron-based spectroscopies at the microscale (SR micro-XRF and micro-XANES/-EXAFS), indicated that Fe^{3+}, in contrast to $^{[6]}Cr^{3+}$, is not exclusively a component of the diaspore structure. While Cr^{3+} substitutes Al^{3+} in octahedral sites of diaspore ($^{[6]}Cr^{3+} \leftrightarrow {}^{[6]}Al^{3+}$), the electron microscopy in nanoscale (TEM-EDS & EELS) revealed that Fe exists in the form of peculiar Fe^{3+}-bearing nanominerals (most likely maghemite-type phases) between 25 and 45 nm in size, in addition to the Fe^{3+} ions substituting Al^{3+} in the diaspore structure. Moreover, it was proven that TiO_2 polymorph mineral nanoparticles, particularly rounded anatase mesocrystals and nanocrystals and individual needle-shaped rutiles, are dispersed into the diaspore matrix. Thus, diaspore in the studied bauxite concerns -in fact- a distinct Fe^{3+}-Cr^{3+}-AlOOH low-T authigenic phase, demonstrated for the first time in literature. On the other hand, the observed TiO_2 mineral nanoparticles (formed, together with diaspore, during diagenesis) and Fe nanominerals (formed during epigenesis) were hitherto unknown not only for the allochthonous karst-type bauxite deposits of Greece, but also for the overall bauxite deposits, worldwide.

© 2016 Elsevier B.V. All rights reserved.

1. Introduction

1.1. Nanogeoscience in ore mineralogy and scope of the present study

According to the fundamentals of nanogeoscience, mineral nanoparticles are the nanoscale-versions of common minerals (exhibiting, however, different physicochemical properties compared to the micro- and macro-scale analogues) whereas nanominerals are distinct phases existent only in nanoscale systems without equivalents at larger scale systems (Hochella, 2002a, 2002b; Hochella, 2006; Hochella, 2008; Hochella et al., 2008; Hochella et al., 2012; Plathe et al., 2010; Schindler and Hochella, 2016; Waychunas and Zhang, 2008). In this case, naturally occurring nanoclusters, polyphasic nanominerals, nanoporous phases, amorphous nanomaterials, amorphous-nanocrystalline transitional phases, surface-disordered nanoparticles, and mesocrystals, all related to the natural progressive transition between amorphous and crystalline materials, have to be considered as well (Caraballo et al., 2015).

The nanogeoscience issues, particularly nano-mineralogy and nano-geochemistry, have emerged into the ore mineralogy and geochemistry field, revealing that large-scale ore systems may be controlled significantly by unknown parameters via the nano-scale ore-processes (e.g.,

Ciobanu et al., 2014; Reich et al., 2011). The necessity for the consideration given to different scales in the study of ore deposits with regard to sulfides has recently been approved by articles. For instance, it has been demonstrated that the old-standing problem of "invisible Au" in pyrite, arsenian pyrite and arsenopyrite, and of other elements (e.g., Ag, Pb and Te), as well as of "colloidal Au", could finally be resolved by applying micro-/nano-mineralogical and nano-geochemical methodologies (Barker et al., 2009; Ciobanu et al., 2012; Ciobanu et al., 2011; Deditius et al., 2011; Fougerouse et al., 2016; Reich et al., 2006; Hough and Noble, 2010; Hough et al., 2008; Hough et al., 2011; Hough et al., 2012; Koneev et al., 2010; Palenik et al., 2004; Pačevski et al., 2012). There are also studies on nanoparticles of Zn-phases from disseminated mineralization of metasomatic rocks in the Dukat ore field in Russia (Filimonova and Trubkin, 2008), as well as magnetite nanoparticles in the mineralized zones of the Pena Colorada Fe-ore deposit in Mexico (Rivas-Sánchez et al., 2009), both indicating that the mineral macro- and nano-sized dependence reflects the formation stages of ore-forming systems. The latest data, yielded by Reich et al. (2013), revealed the distribution of precious metals, metalloids and heavy metals in nano-scale of pyrite crystals from the Dexing porphyry Cu deposit (China). Furthermore, proof of the existence of PGE-bearing arsenide and sulfide nanocrystals of the Merensky Reef PGE-ore deposit of the Bushveld complex in South Africa have been provided by Wirth et al. (2013). Recently, another study (Helmy et al., 2013) showed that the pre-existing noble metal nanophases, nanoclusters, and nanoparticles, preceding the formation of stable phases in natural complex systems, are the building blocks. At the same time, the importance of nano-mineralogy and -geochemistry in the case of phosphate ore deposits and non-sulfide supergene ores, namely Zn-clays, has been underscored by Cosmidis et al. (Cosmidis et al., 2013) and Mondillo et al. (Mondillo et al., 2015), respectively.

Bauxite ore deposits remain the main source of Al metal for industry and society. Among various types of bauxites, the karst-type deposits are characteristic for Eurasia (including the Mediterranean and Balkans), the Caribbean, the Eastern US and Oceania (Bárdossy, 1982). The economically important European karst-type bauxite deposits are situated in the mining area of the Parnassos-Ghiona Mountains in central Greece (Fig. 1). The Greek mining industry controls the most significant bauxite reserves in the European Union (U.S. Geological Survey, 2015). In addition, the European Commission recommended that Al and bauxite are of high "economic importance" and decreased "supply risk" values (EU Ad-hoc Working Group, 2014). The nano-mineralogical and -geochemical investigation of karst-type bauxite ore deposits have not adequately been demonstrated in any literature. After the pioneering works by Bárdossy and Mack (1967) and, later, by Bárdossy and White (1979), who presented transmission electron microscopic (TEM) images of bauxite minerals from karst-type bauxites for the first time, only recently Gan et al. (2013) has presented TEM images of mineral nanoparticles from karst-type bauxites of northern Europe and Jamaica. Bárdossy (1982) presumed that colloid geochemistry (colloidal systems, i.e. nanoparticles) rules the Al-ore (bauxite) deposits, concerning natural low-T inorganic nanomaterials made of dispersed-phase particles. A microscale investigation of Greek karst-type bauxite using laser ablation inductively-coupled plasma mass spectrometry (LA-ICP-MS) and Synchrotron radiation (SR) techniques, such as micro-X-ray fluorescence (micro-XRF) and micro-X-ray absorption near edge structure/-extended X-ray absorption fine structure spectroscopy (micro-XANES/-EXAFS) has recently been carried out towards the Th partitioning and speciation (Gamaletsos, 2014; Gamaletsos et al., 2011). A relevant Zr K-edge XAFS investigation has been performed for non-karstic bauxites (lateritic) from Brazil (Douvallet et al., 1999).

The scope of the present study is to combine, for the first time in literature with regard to the karst-type bauxites of Greece and worldwide, diffraction (powder X-ray diffraction: PXRD), spectroscopic (^{57}Fe Mössbauer, SR micro-XRF, micro-XANES/-EXAFS), magnetic susceptibility

measurements and electron microscopic techniques (i.e., scanning electron microscopy equipped with an energy dispersive spectrometer: SEM-EDS; scanning TEM mode in SEM: STEM mode using EDS in the SEM; TEM-EDS &electron energy-loss spectroscopy: EELS) for a detailed mineralogical and geochemical characterization and, additionally, the study of mineral nanoparticles and nanominerals in high-grade karst-type bauxite (Al-rich and Fe-depleted samples; Al_2O_3 ca. 80 wt.%) from active mines of the Parnassos-Ghiona area in central Greece. Furthermore, it is a new attempt to improve the existing geological knowledge related to the formation of the high-grade diasporic karst-type bauxite based on nano-mineralogical and -geochemical issues. Finally, it is critical to mention that nanominerals and mineral nanoparticles occurring in karst-type bauxite, partially contribute to the formation (during metallurgy; the so-called "Bayer process") of novel Th-hosting nano-perovskite phases, having a technological and environmental significance (Gamaletsos et al., 2016).

2. Geological settings end economic characteristics of karst-type bauxite deposits of Parnassos-Ghiona mines

The allochthonous karst-type bauxite deposits of the Parnassos-Ghiona mountains (central Greece), which belong to the Mediterranean bauxite belt (e.g., Bárdossy, 1982; Valeton, 1972; Valeton et al., 1987), are hosted within Mesozoic (Upper Triassic–Upper Cretaceous) carbonate formations of the Parnassos-Ghiona geotectonic zone. Three bauxite horizons (from bottom to top: B1, B2 and B3; see upper image of Fig. 1) can easily be distinguished (Arp, 1985; Biermann, 1983; Gamaletsos, 2014 and references therein; Nia, 1968; Valeton et al., 1987). The lower (B1) horizon is now inactive; the active mines are restrictively situated in the intermediate (B2) and the upper (B3) bauxitic horizons, which are currently fully operated by Greek mining industry and particularly by "Aluminium of Greece S.A.".

Greece is the 12th largest bauxite mine producer worldwide, but also the largest in the EU with an annual production of 2100 thousand metric dry tons in 2011 (U.S. Geological Survey, 2015). At the present time, the Greek karst-type bauxite reserves, which could be produced economically, are estimated to be approximately 600,000 thousand metric dry tons. Most of the raw material is processed by the "Aluminium of Greece S.A." at its industrial complex at Aghios Nikolaos (Antikyra, Corinth gulf) for the production of alumina (800 thousand metric dry tons; U.S. Geological Survey, 2015) and metallic aluminium (165 thousand metric dry tons, see: Tsirambides and Filippidis, 2012a, 2012b) used in industry and construction. According to the U.S. Geological Survey, Greece is now considered to be the 16th largest alumina producer in the globe, and the 4th among the EU member-states.

The main mineralogical and geochemical characteristics of the Parnassos-Ghiona bauxite deposits have been reported in numerous studies using various conventional microscopic and analytical methods, together with more detailed characterization techniques such as instrumental neutron activation analysis (INAA), carbon, sulfur and oxygen isotopic analysis (e.g., Gamaletsos, 2014 and references therein; Gamaletsos et al., 2007; Gamaletsos et al., 2011). In general, previous works on karst-type bauxites from the Mediterranean bauxite belt gave emphasis to the trace element distribution of selective samples (Özlü, 1983) and the conditions related to the formation of the deposits (Kalaitzidis et al., 2010; Valeton et al., 1987; Öztürk et al., 2002). Concerning the Parnassos-Ghiona bauxites, only the basic (in macro- and micro-scale) mineralogy and geochemistry have been investigated, with the exception of the general geology (Gamaletsos, 2014 and references therein).

3. Materials and methods

3.1. Samples

This study draws on high-grade karst-type bauxite samples originating from active mines located within the B3 bauxite horizon of the
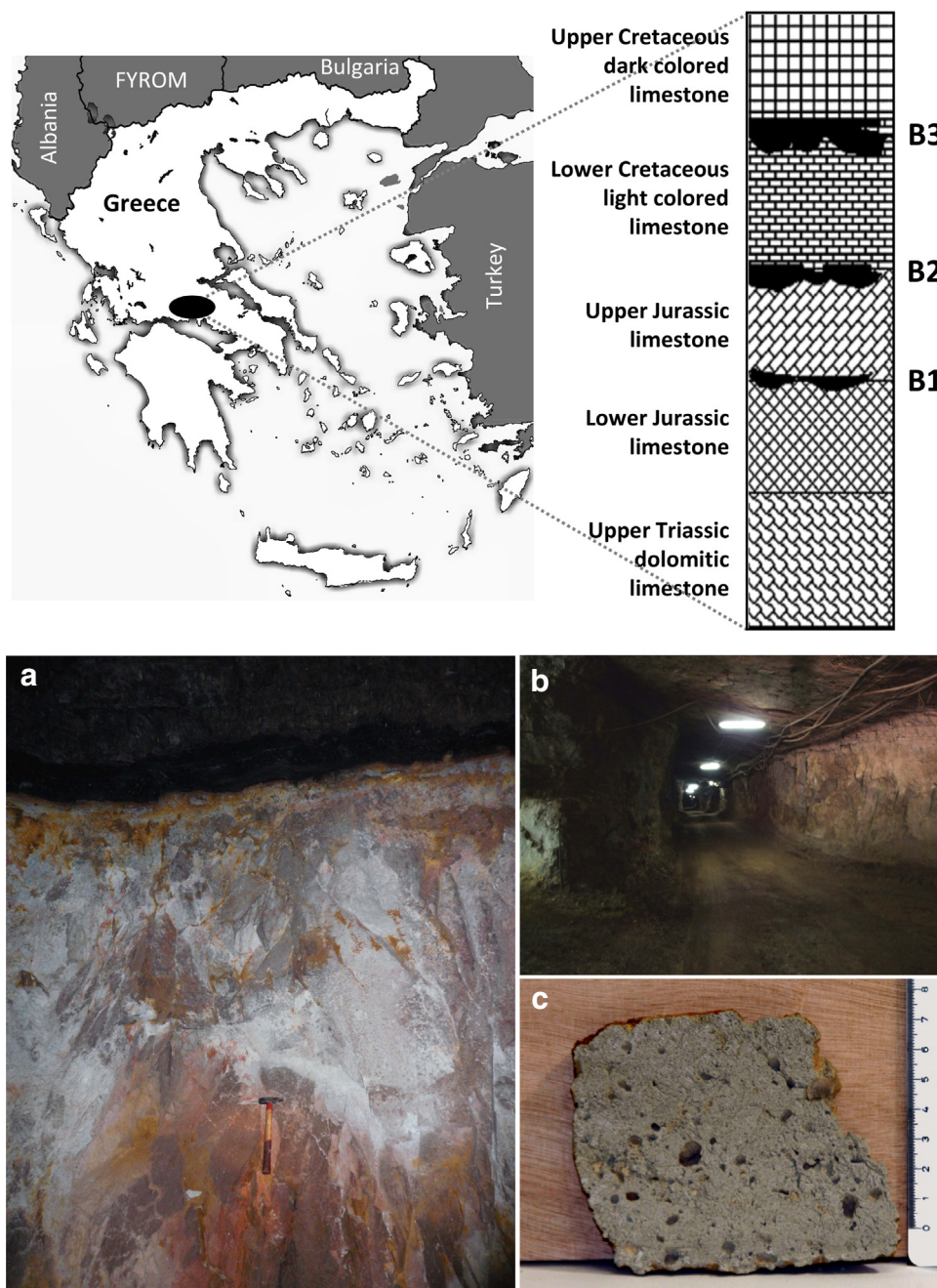
Fig. 1. Upper image: The location of Parnassos-Ghiona active mines in Greece and a simplified stratigraphic position of B1 (lower), B2 (intermediate) and B3 (upper) bauxite horizons (modified after Valeton et al., 1987). Lower image: Representative underground mining front at Pera-Lakkos mines located at B3 horizon, where the high-grade karst-type bauxite was sampled below the coal layer (Kalaitzidis et al., 2010) intercalated between the bauxite and the dark colored hanging-wall limestone (a); general view of the underground works leading to the mining front (b); typical sample of white-grey high-grade diasporic karst-type bauxite (Al-rich and Fe-depleted) used in the present study (c).

Parnassos-Ghiona area (Fig. 1). This type of Al-ore is representative of typical Greek industrial bauxite, which is Fe-depleted or "bleached" (white-grey in color) and contains an average of ca. 80 wt.% Al_2O_3, in bulk. The main constituent, supplying Al in the metallurgy, is diaspore, whereas there is also anatase (TiO_2 polymorph) hosting a significant number of actinide elements (mainly Th and less U) and also high-field strength elements/HFSE (Nb, Ta) as has been indicated by LA-ICP-MS and Synchrotron-based techniques previously (Gamaletsos, 2014; Gamaletsos et al., 2011). The specimens, used to investigate the nano-mineralogy and -geochemistry of Greek bauxite, were collected from underground mining sites (Pera-Lakkos mines; Fig. 1) of the "Aluminium of Greece S.A.". The samples finally subjected to laboratory microscopic and spectroscopic measurements, were composite mining

materials, created by following standard mixing procedures and sample splitters, by taking the appropriate number of specimens vertically at mining fronts (Fig. 1). Such composite samples are typically obtained by mining companies for industrial minerals characterization, to be used as commercial products.

3.2. Powder X-ray diffraction

The bulk mineralogical composition was determined by means of PXRD using a Bruker AXS D8 ADVANCE diffractometer (CuK$_\alpha$ radiation, dwell time of 8 s per 2θ step with a step of 0.02°). Furthermore, the Rietveld method has been attempted to define the lattice constants of the crystalline phases present in the sample using the GSAS (Larson

and Von Dreele, 2004) as well as the FullProf (Rodríguez-Carvajal, 1993) refinement software packages.

3.3. Electron microscopy in microscale and mesoscale

The investigation of the mineralogical and the chemical composition at the microscale was conducted using an FEI Quanta 200 FEG SEM equipped with EDS. The SEM QFEG observations were conducted under low-vacuum (using pressure at 50 Pa and accelerating voltage at 15 keV) in the case of EDS elemental mapping and high-vacuum conditions (using pressure at 10^{-4} Pa and accelerating voltage at 20 keV). Moreover, a bright-field (BF) STEM mode in the SEM QFEG (accelerating voltage at 30 kV and working distance at 10 mm) was additionally used in order to define the elemental distribution in the diasporic matrix at the mesoscale (Caraballo et al., 2015; Heaney, 2015).

3.4. ^{57}Fe Mössbauer and magnetic susceptibility measurements

The ^{57}Fe Mössbauer spectra of the samples were recorded in transmission geometry at 300 K and 10 K using a constant-acceleration Mössbauer spectrometer equipped with a ^{57}Co (Rh) source kept at room temperature (RT) and a closed loop He cryostat (ARS). The susceptibility measurements were conducted on an AGICO MFK1 kappa bridge with cryostat and furnace attachments, allowing acquisition over a temperature range from approximately −200 °C to 700 °C in an AC field of 200 A/m and a frequency of 976 Hz. Multiple specimens of powdered bauxite were analyzed, some in heating runs that spanned the full temperature range, and others in more complex sequences where the same sample was heated iteratively to initially moderate and then progressively higher temperatures, followed by cooling it between each run. Heating runs were conducted in air to minimize the formation of reduction products (notably magnetite) that may be produced from natural samples in "inert" argon atmospheres.

3.5. Synchrotron Radiation (SR) investigation (micro-XRF/-XANES/-EXAFS) and Laser micro-Raman observation in microscale

The mineralogy of the bauxite micro-areas, to be subjected to Synchrotron Radiation (SR) study, was previously checked by reflected-light microscopy and Laser micro-Raman spectroscopy. The spectra were obtained on the polished sections using a Kaiser RXN1 Analyzer portable Laser micro-Raman spectrometer equipped with two-wavelength excitation lasers (at 532 nm and 785 nm). XAFS spectra in microscale (micro-XANES/-EXAFS) were obtained at SUL-X beamline of ANKA Synchrotron, KIT, Germany. The spectra were obtained in micro-areas, previously selected by optical microscopy, Laser micro-Raman and SR micro-XRF. Special care was given to avoid possible detrital Cr-spinel microcrystal fragments, which could interfere with spectroscopic data regarding Cr. Typical Cr^{3+} and Cr^{6+} compounds and minerals were used as reference materials. The XAFS measurements were carried out at room temperature in both fluorescence and transmission mode. Energy was calibrated for the Cr K-edge XAFS measurements to 5989 eV (1st derivative of the Cr K-edge, Cr metal foil between the ionization chambers 2 and 3). The spectra were processed using the ATHENA and the ARTEMIS software packages (Ravel and Newville, 2005). For the overall EXAFS fitting procedure, structural data from a grimaldiite (α-CrOOH) reference from the literature (Christensen et al., 1977) were imported from its atoms.inp file for the FEFF calculation. This reference was used as a "Cr-analogue" of diaspore (α-AlOOH) and, particularly, for the EXAFS fitting of the first shell parameters, depicting the Cr—O bonds into the diaspore of the studied bauxite.

3.6. Electron microscopy in nanoscale

The TEM-EDS & EELS measurements were carried out using an FEI Tecnai F20 FEG TEM operated at 200 kV and an FEI Titan 80-300ST FEG TEM operated at 300 kV. Energy-filtered TEM for O, Ti and Fe and EELS were obtained using a Gatan imaging filter equipped to the Titan TEM. The EELS data were acquired with an energy dispersion of 0.2 eV/pixel and an energy resolution of 0.8 eV. Qualitative TEM-EDS measurements were carried out using an electron beam with <10 nm in size. The bauxite samples were polished down to approximately 30 μm, thinned to electron transparency using Ar ion milling, and coated lightly with carbon.

4. Results and discussion

4.1. Bulk mineralogical composition

According to the PXRD patterns (Fig. 2), the studied high-grade diasporic karst-type bauxite contains diaspore (α-AlOOH polymorph), anatase and minor rutile (TiO_2 polymorphs) as major crystalline phases. The presence of diaspore (α-AlOOH) as the only AlOOH polymorph in the studied sample was also checked by Laser micro-Raman spectra giving the characteristic peak at 448 cm^{-1}, which is in accordance with previous studies (Gamaletsos, 2014; Gamaletsos et al., 2007). Accessory minerals, such as detrital zircons, as well as Cr-spinels and REE-fluorocarbonates (Gamaletsos, 2014 and references therein; Gamaletsos et al., 2011), occurring as rare irregular microcrystals and aggregates into the diaspore matrix, were not detected by PXRD. The Rietveld refinement of the PXRD patterns yielded the unit cell parameters of the α-AlOOH and TiO_2 phases (Table 1), which are in agreement with the values reported in literature (Cromer and Herrington, 1955; Hazemann et al., 1991; Howard et al., 1991; Hummer et al., 2007; Klug and Farkas, 1981). Thus, it can be argued that there is no significant distortion of the diaspore unit cell, despite the presence of metal impurities, namely Fe and Cr, revealed by electron and Synchrotron-based microanalyses (see the 4.2 & 4.4 subsections). Moreover, the unit cell of anatase also remains rather undistorted regardless of the incorporation of HFSE, such as Th, U, Nb, and Ta (Gamaletsos, 2014; Gamaletsos et al., 2011).

4.2. Mineralogical and chemical composition at the microscale

The SEM-EDS data showed the dominance of AlOOH (diaspore according to PXRD) in the matrix, and dispersed anatase and zircon grains in microscale (Fig. 3), as well as individual Cr-spinel crystal fragments (not shown herein, see: Gamaletsos, 2014). Zircon and Cr-spinel are detrital minerals transferred from weathered parent rocks during the bauxitization processes at low temperature (low-T), while minor REE
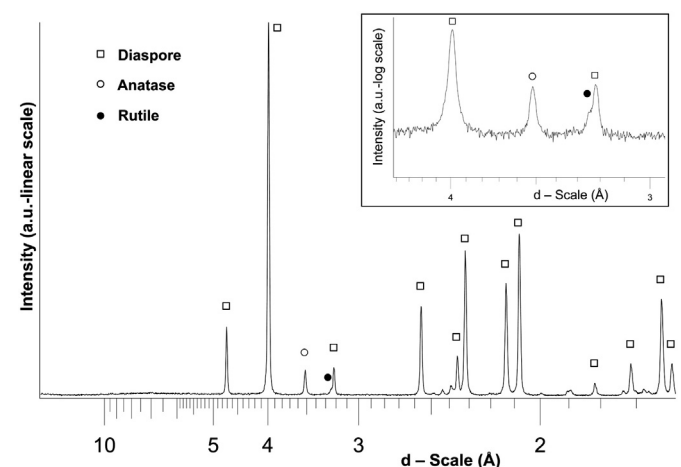
Fig. 2. Powder XRD pattern (d scale in Å) of high-grade karst-type bauxite showing the presence of diaspore (α-AlOOH), anatase, and rutile, indicated by open square (□), circle (○), and solid circle (●) symbols, respectively. The inset image, in logarithmic scale, indicates the rutile peak overlapping with diaspore.

Table 1
Unit cell parameters of diaspore, anatase, and rutile in high-grade diasporic karst-type bauxite from Parnassos-Ghiona mines, yielded by Rietveld method using the GSAS (Larson and Von Dreele, 2004) and the FullProf (Rodríguez-Carvajal, 1993) refinement software packages (see also Fig. 2).

| Refinement software	Mineral	Space Group	a (Å)	b (Å)	c (Å)	Weight (%)	Cell Volume (Å^3)	R values	
								Rwp	Rp
GSAS	Diaspore	*Pbnm*	**4.402554** (0.000078)	**9.424099** (0.000144)	**2.845213** (0.000056)	96.603 (4.71544)	118.048		
	Anatase	*I41/amd*	3.783301 (0.000368)	3.783301 (0.000368)	9.502564 (0.002090)	3.1342 (4.3628)	71.902		
	Rutile	*P42/mnm*	4.590689 (0.001167)	4.590689 (0.001167)	2.958973 (0.002198)	0.26286 (0.37694)	27.167		
								0.088	**0.0678**
FullProf	Diaspore	*Pbnm*	4.40511 (0.00004)	9.43015 (0.00008)	2.84717 (0.00003)	98.95 (0.75)	118.274		
	Anatase	*I41/amd*	3.78660 (0.00016)	3.78660 (0.00016)	9.50218 (0.00080)	0.39 (0.01)	71.962		
	Rutile	*P42/mnm*	4.59424 (0.00059)	4.59424 (0.00059)	2.95845 (0.00074)	0.66 (0.05)	27.184		
								0.128	0.0966

fluorocarbonate mineral aggregates (not shown here, see: Gamaletsos, 2014 and references therein; Gamaletsos et al., 2011) might be considered authigenic (e.g. Bárdossy, 1982; Valeton, 1972; Valeton et al., 1987). It should be emphasized that the diaspore matrix contains, except for Ti (corresponding in fact to anatase inclusions), a rather homogeneous distribution of detectable quantities of Fe and Cr (see EDS spectrum and linescan in Fig. 3). That implies a novel low-T natural Fe-Cr-AlOOH mineral and two possible Fe forms: Fe ions in the structure of diaspore and potential Fe mineral nanoparticles and/or nanominerals. Titanium is inhomogeneously dispersed into the diaspore matrix, always resulting in a negative relation to Al. This can be attributed to occluded Ti minerals (TiO_2 polymorphs) in microscale (Fig. 3) or, even, to the presence of Ti mineral nanoparticles and/or nanominerals, rather than to a distinct "Fe-Cr-Ti-AlOOH phase". Therefore, detailed electron microscopic studies at the mesoscale and nanoscale (SEM-STEM and TEM-EDS & EELS), complemented by ^{57}Fe Mössbauer and X-ray spectroscopies, were performed to examine the above findings (see the 4.3, 4.4 and 4.5 subsections).

4.3. Fe solid-state speciation and magnetic susceptibility

The ^{57}Fe Mössbauer spectra of the high-grade diasporic karst-type bauxite are presented in Fig. 4 and the resulting Mössbauer parameters from the best fits of these spectra using the IMSG code (Douvalis et al., 2010) are listed in Table 2. The spectra were analyzed using a combination of two quadrupole split doublets and two magnetically split components. The quadrupole doublets are well resolved, but the magnetic components possess large line broadening (we allowed a spreading of hyperfine magnetic fields ΔB_{hf} for each component to describe this broadening), indicating that they correspond to Fe containing phases with either reduced particle size and/or low crystallinity. That implies the presence of Fe mineral nanoparticles and/or Fe nanominerals as also being suggested by the electron microscopic data. The isomer shift (IS-given relative to α-Fe at 300 K) and quadrupole splitting (QS) values of the major quadrupole split doublet indicate that the main contribution originates from paramagnetic Fe^{3+} ions, while the second paramagnetic minor component with large IS and QS values is attributed to Fe^{2+} ions; the IS values of both magnetic components correspond to Fe^{3+} ions (Cornell and Schwertmann, 2003; Dyar et al., 2006; Fysh and Clark, 1983; Hill et al., 1978; Kotova et al., 2015; Kuzmann et al., 2003; Murad, 2005; Raj et al., 1993). It is, therefore, argued that the recorded major Fe^{3+} component corresponds to Fe-Cr-diaspore (Fe-Cr-AlOOH where Fe^{3+} substitutes for Al^{3+} ions in octahedral sites, i.e. $^{[6]}Fe^{3+} \leftrightarrow {}^{[6]}Al^{3+}$) and to potential occluded Fe^{3+} mineral nanoparticles and/or nanominerals. The latter results are claimed to be responsible for the presence of the magnetic component with the high hyperfine magnetic field (B_{hf}) in the spectra, constituting ferrimagnetic minerals with large Fe content, most probably of maghemite-type (γ-Fe_2O_3) (Cornell and Schwertmann, 2003). The magnetic component with the collapsing B_{hf} characteristics in both spectra is attributed to either not well crystallized nano-maghemite or Fe^{3+} dispersed in amorphous minor phases not detected by PXRD. A part of these types of phase acquires
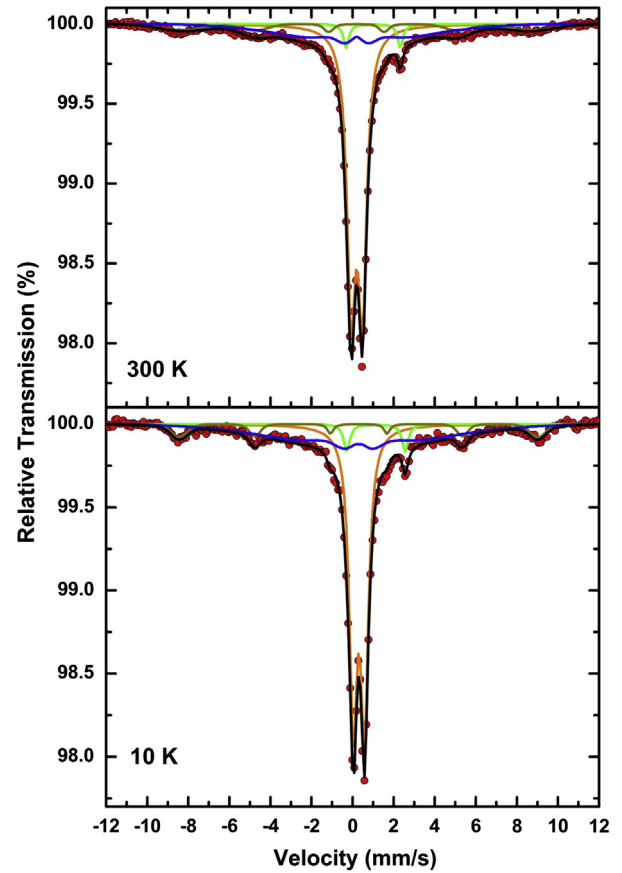
superparamagnetic characteristics (Culltity and Graham, 2009) at 300 K due to their reduced sizes and thus cannot be distinguished from the pure paramagnetic Fe^{3+} substitutes for Al^{3+} ions in the octahedral sites of diaspore. However, when the temperature drops to 10 K the cessation of the superparamagnetic relaxation for these phases leads to the increase of the absorption area of the B_{hf} collapsing component and to the corresponding decrease of the absorption area of the main paramagnetic component (see Table 2). Regarding the Fe^{2+}-bearing phase in the sample with a minor absorption area of ca. 4% both at 300 and 10 K, its most possible origin could be ascribed to microcrystal fragments of (detrital) Cr-spinels (Gamaletsos, 2014).

The examination of magnetic transitions during temperature cycling is a diagnostic method to observe even low concentration of magnetic minerals. These transitions manifest as abrupt increases or decreases in magnetization and/or magnetic susceptibility when the sample is heated or cooled through a critical temperature. The primary feature of the mass-normalized magnetic susceptibility measurement for the high-grade diasporic karst-type bauxite, presented in Fig. 5 (upper image), is the irreversibility of the susceptibility after heating the sample to approximately 700 °C. When heating above 500 °C, the susceptibility begins to increase before dropping sharply to just below 600 °C. During the cooling run, the susceptibility increases as the sample is cooled through 600 °C and remains higher than its initial values. There is a similar but smaller and less abrupt increase as the sample is cooled through approximately 235 °C; a small deviation at a similar temperature can be observed in the heating run but magnitude has greatly been enhanced by the time exposed at high temperature. The two abrupt changes in magnetic susceptibility described above indicate two magnetic phases, which either increase in quantity or undergo some magnetic enhancement as a function of heating. The lower temperature transition (~235 °C) is very close to the Curie temperature of Fe_2CrO_4 (Francombe, 1957), i.e. Cr-spinel that is present as accessory mineral (Gamaletsos, 2014). The Curie temperature as calculated by the point of maximum slope (Tauxe, 1998) is slightly above 200 °C, that of pure Fe_2CrO_4, suggesting a slight deviation from end-member composition. The phase that shows a higher temperature transition (Culltity and Graham, 2009) seems more uncertain, as the Curie temperature of the phase produced during heating is indistinguishable between those of pure magnetite (Fe_3O_4) and maghemite 585–590 °C (Culltity and Graham, 2009). Also there are notably no further magnetic transitions above 600 °C that would indicate the presence of hematite (α-Fe_2O_3), which can remain stable in high temperatures with the presence of Al. Neither the initial (unheated) low-temperature measurements nor those acquired after the high-temperature run show any magnetic transitions below room temperature that would indicate primary or secondary magnetite or end-member hematite. The Verwey transition at ca. − 150 °C (~120–125 K, see: Verwey, 1939) is diagnostic of magnetite, but is difficult to be observed in susceptibility measurements of single-domain carriers (Muxworthy, 1999). It may also be suppressed by even small degrees of cation substitution (Kakol et al., 1992) or non-stoichiometry (Aragón et al., 1985). Thus, the inability to identify any inflections in the susceptibility curve in this temperature range does
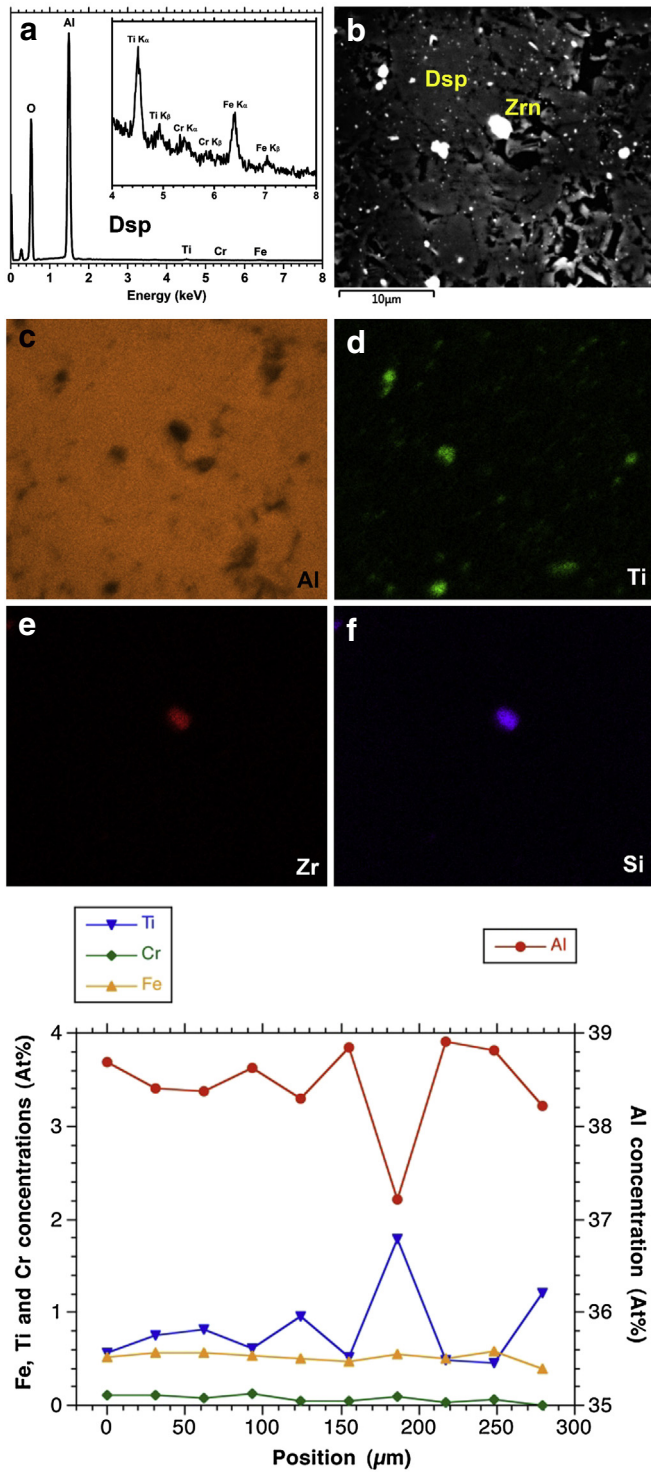
Fig. 3. Upper: SEM-EDS data (a: EDS spectrum of diaspore/Dsp and enlarged energy area of the spectrum showing the presence of Ti together with Cr and Fe in the diaspore matrix; b: BSE image of a characteristic micro-area containing also a zircon/Zrn grain; c–f: elemental maps for Al, Ti, Zr and Si). Lower: Representative SEM-EDS linescan for Al, Fe, Ti, and Cr, in a selected region of diaspore matrix.

Fig. 4. ^{57}Fe Mössbauer spectra recorded at room temperature (300 K; upper image) and at 10 K (lower image) concerning the investigated high-grade diasporic karst-type bauxite.

not rule out magnetite as the phase created at high-temperature, but on the other hand, this phase is not detected in the Mössbauer spectra of the sample. The Morin transition of hematite, which occurs at approx. − 10 °C (Morin, 1950) is likewise diagnostic of the presence of that mineral; the lack of any magnetic transitions at this temperature or at the Neel temperature of 675 °C indicate that there is no hematite initially

present or generated during the heating run. These results, regarding the Fe-bearing phases in the sample, are in agreement with the results obtained from Mössbauer spectroscopy analysis. The lower image of Fig. 5 shows the repetition of the susceptibility measurements by cycling to increasing temperature in order to observe the point at which alteration in the sample becomes irreversible. The heating and cooling curves appear similar up to a maximum temperature of 510 °C, after which increasing amounts of ferromagnetic material is produced and the susceptibility curves become dissimilar. The onset of alteration occurs at a notably higher temperature than that of the dehydroxylation of potential Fe-oxyhydroxide precursors, such as lepidocrocite, ferrihydrite, and goethite, which has been observed at temperatures as low as 200 °C (e.g., Gendler et al., 2005). This higher temperature is similar to that of the inversion of maghemite and Ti-substituted maghemite; while a range of inversion temperatures have been reported, the onset above 510 °C corresponds precisely to the values reported in at least one study (Özdemir and Banerjee, 1984). The Curie temperature of the ferrimagnetic phase generated at high temperatures is strongly suggestive of maghemite, but the precursors are less certain. The increase in susceptibility suggests either a compositional or a crystallographic change, and the nature of that change might indicate the starting material. The susceptibility curves are qualitatively very similar to magnetization measurements acquired during the inversion of Ti-substituted maghemite (Readman and O'Reilly, 1970; Özdemir, 1987), a process that produces pure magnetite and a weakly-magnetic second phase. A second possibility for the development of ferrimagnetic maghemite is a minor crystallographic change from a non-magnetic maghemite precursor or through size growth of very small superparamagnetic or amorphous mineral nanoparticles and/or nanominerals during heating. This lack of magnetic signals could be caused by the amorphous nature

Table 2
[57]Fe Mössbauer parameters resulted from the best fits of the spectra at 300 K and at 10 K (see Fig. 4). IS is the isomer shift (relative to a-Fe at 300 K), $\Gamma/2$ is the half line-width, QS is the quadrupole splitting, 2ε is the quadrupole shift, B_{hf} is the central value of the hyperfine magnetic field, ΔB_{hf} is the spreading of B_{hf}, and A is the relative spectral absorption area of each component, whose assignment are discussed in the text and listed here briefly. Typical errors: ± 0.02 mm/s for IS, $\Gamma/2$, 2ε and QS, ± 3 kOe for B_{hf} and $\pm 3\%$ for A; Uncertainties: IS, $\Gamma/2$, 2ε, QS, ± 0.02 mms^{-1}, $B_{hf} \pm 5$ kOe, Area $\pm 3\%$.

| | | IS | | | | | | | | Fe^{3+}/ΣFe |
| | T | (α-Fe) | $\Gamma/2$ | 2ε or QS | B_{hf} | ΔB_h | Area | | Fe | |
Sample	K	mms^{-1}	mms^{-1}	mms^{-1}	kOe	kOe	%	Component assignment	valence	%
High-grade diasporic karst-type bauxite from Parnassos-Ghiona mines	300	0.31	0.25	0.55	0	0	64	Fe^{3+} substituting Al^{3+} in diaspore & in superparamagnetic nano-maghemite and amorphous phases	3+	96
		1.11	0.16	2.64	0	0	4	Fe^{2+} in (detrital) Cr-spinel	2+	
		0.30	0.14	0.00	531	62	10	Fe^{3+} in maghemite-type phase	3+	
		0.31	0.14	0.00	210	138	22	Fe^{3+} in nano-maghemite and amorphous phases	3+	
	10	0.41	0.22	0.55	0	0	56	Fe^{3+} substituting Al^{3+} in diaspore	3+	
		1.25	0.18	2.84	0	0	4	Fe^{2+} in (detrital) Cr-spinel	2+	
		0.40	0.15	-0.01	542	20	9	Fe^{3+} in maghemite-type phase	3+	
		0.41	0.15	0.01	245	180	31	Fe^{3+} in nano-maghemite and amorphous phases	3+	
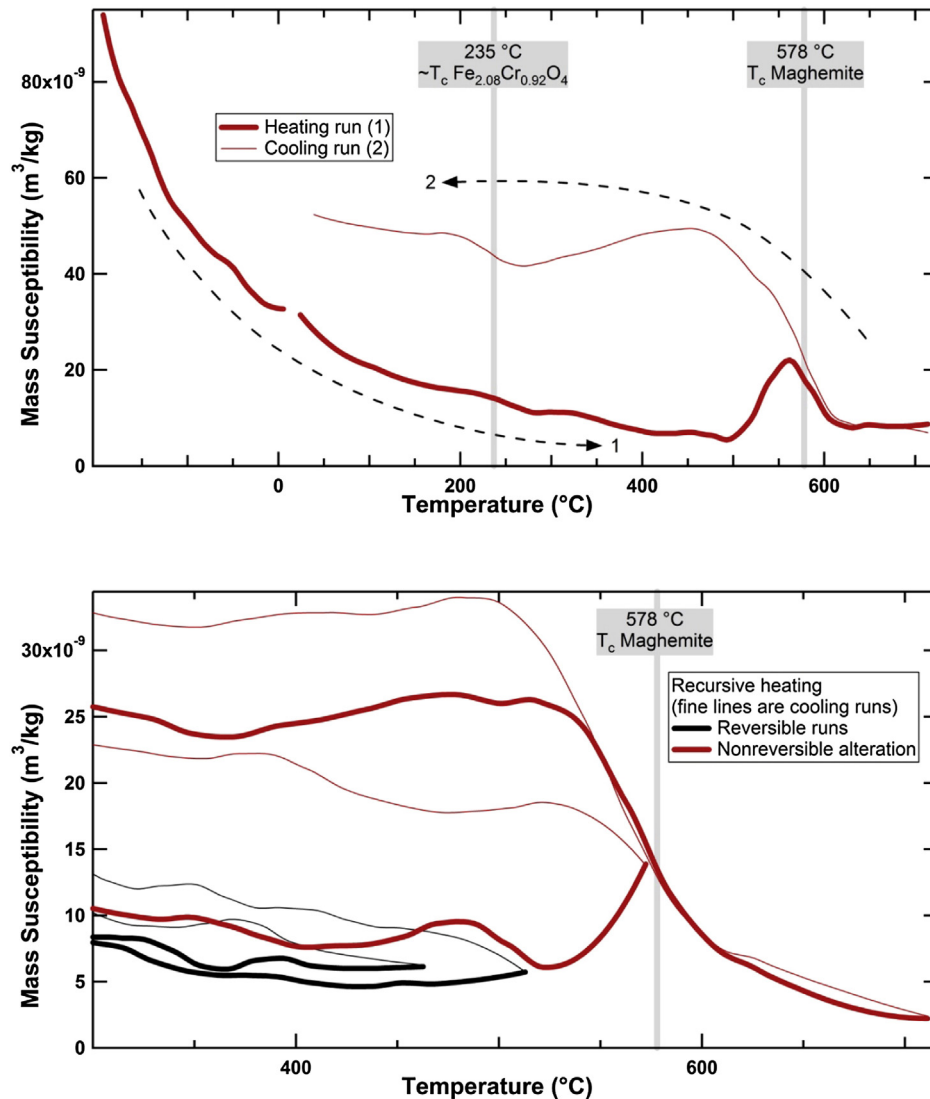
Fig. 5. Magnetic susceptibility versus temperature measurements. Upper image: Full temperature run, illustrating measurement protocol of heating run from -192 °C to 700 °C, followed by cooling to room temperature. Both maghemite and (detrital) Cr-spinel are present after heating to high-temperature, indicating a chemical or structural change from some undetermined precursor (most likely the Fe nanominerals); lower image: Recursive heating of the same sample to progressively higher temperatures to establish critical temperature of maghemite development. Heating up to 510 °C produces little irreversible change, but the successive run to 560 °C (of which a total of 13 min between 510 and 560 °C) causes the formation of maghemite, a process which continues in further runs to yet, higher temperatures.

of these phases or with a sufficiently defect-rich lattice due to the very small size of these mineral nanoparticles and/or nanominerals, causing their magnetization to reduce significantly and the particles to exhibit superparamagnetic behavior (Culltity and Graham, 2009). Upon heating, the development of crystalline ordering from a previously amorphous phase would create a new phase of increased size as well. Alternatively, enhancement of magnetization by annealing might be attributed to consequent suppression of lattice defects that would effectively increase the relaxation time of superparamagnetic particles, generating a magnetic phase that can be observed in laboratory time-scales. This final possibility is suggestive of the presence of Fe nanominerals, implied by the Mössbauer spectroscopy, and directly observed by the study at the nanoscale using TEM-EDS & EELS (see the 4.5 subsection).

4.4. Elemental distribution and Cr speciation at the microscale

Inasmuch as the state of Fe into Fe-Cr-diaspore was illustrated by the Mössbauer spectroscopic study, the samples were further subjected to Synchrotron-based techniques in microscale in order to elucidate the nature of Cr detected by SEM-EDS. Prior to the SR micro-XRF measurements, proper micro-areas on polished sections were logged using an optical microscope in reflected light (Fig. 6 – upper left image). Particular micro-areas were also checked by means of Laser micro-Raman spectroscopy in order to ensure pure diaspore regions for acquisition of micro-XANES/-EXAFS spectra. Emphasis was also given to avoid possible detrital Cr-spinel microcrystal fragments, which could interfere with spectroscopic data regarding Cr. The obtained micro-Raman spectra were compared to a standard Raman spectrum (red and black lines
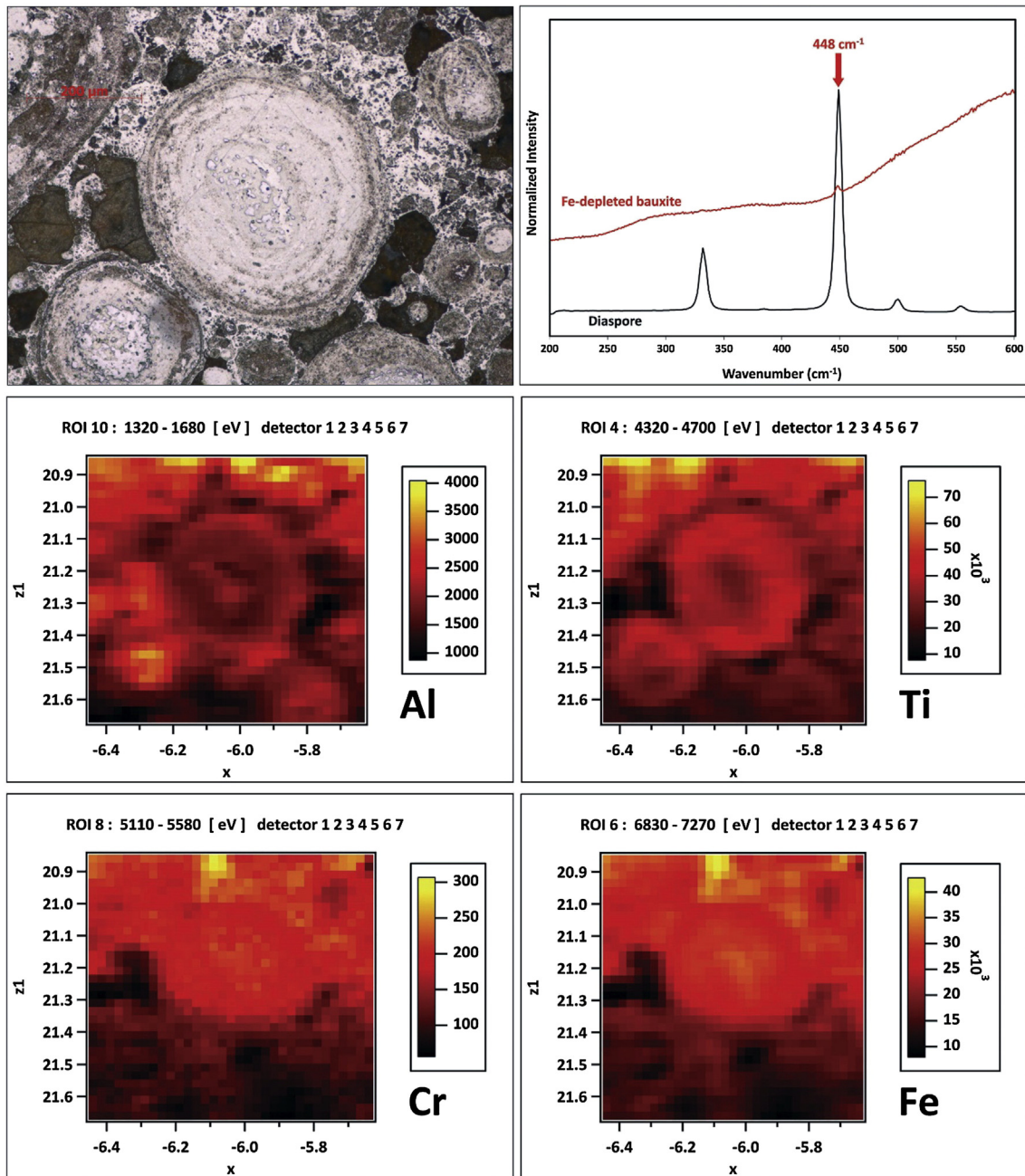

Fig. 6. Optical microscopic -reflected light- image of diasporic pisoliths (upper left image), previously checked for AlOOH polymorphs by Laser micro-Raman spectroscopy (upper right image), studied into the ANKA SUL-X vacuum chamber by SR micro-XRF spectroscopy for achievement of Al, Ti, Cr, and Fe elemental maps (middle and lower images) and acquisition of consequent micro-XANES/-EXAFS spectra (see Figs. 7-9).

respectively in Fig. 6 – upper right image) from the Mineral Spectroscopy Server of CalTech (© Prof. G. Rossman 2006). The Laser micro-Raman investigation was in accordance with previous works (Gamaletsos et al., 2007; Gamaletsos, 2014) that had suggested this quick and accurate laboratory method for distinguishing diaspore from boehmite in the low-wavenumber region (200 cm^{-1}–600 cm^{-1}) with distinct bands of the natural AlOOH polymorphs at 448 cm^{-1} for diaspore and 362 cm^{-1} for boehmite.

The SR micro-XRF maps for major elements (Al, Ti, Cr, and Fe) in the studied high-grade karst-type bauxite are shown in the middle and lower images of Fig. 6. It is evident that Al, Fe and Cr are relatively intercorrelated, whereas Ti exhibits a rather contrasting behavior especially at the center of pisoliths. The Cr K-edge micro-XANES spectra, which were obtained in diasporic regions aiming at the elucidation of Cr oxidation state in diaspore, are presented in Fig. 7. The processing of the spectra and the comparison with reference to Cr^{3+} and Cr^{6+} materials results in Cr^{3+}, logically occupying octahedral sites in the structure of diaspore. The Fourier transform (FT) of χ(k) of the Cr K-edge micro-EXAFS spectrum of diasporic pisoliths (Fig. 8) indicates the similarity of the studied sample and the Cr-oxyhydroxide (grimaldiite-type) reference material. The interpretation of radial distribution functions – RDF spectra (Fig. 9) indicated that the first-shell fitting of Cr^{3+} in Cr^{3+}-(Fe^{3+})-AlOOH can adequately be performed using crystalline grimaldiite reference (Christensen et al., 1976; Christensen et al., 1977). The fitting suggests a value of 1.965 Å for the interatomic distance between the central atom of Cr and the first neighbor of O, which is reasonable for grimaldiite (Cr–O: 1.92–2.07 Å) and also for Al—O bond length in diaspore referred to vary from 1.851 to 1.982 Å (Busing and Levy, 1958; Hill, 1979). Thus, it is demonstrated that chromium exists as Cr^{3+} in the structure of diaspore, substituting Al^{3+} in octahedral sites ($^{[6]}$Cr^{3+} ↔ $^{[6]}$Al^{3+}) as stands in the case of Fe^{3+}. The coexistence of Cr^{3+} and Fe^{3+} in low-T (sedimentary) authigenic diaspore from karst-type bauxite mines of the Mediterranean bauxite belt (e.g., Bárdossy, 1982; Valeton, 1972; Valeton et al., 1987) is demonstrated for the first time in literature. Previous works had mentioned the existence of only Cr^{3+} in diaspore, based on luminescence and EPR measurements (Meil'man and Torchinskii, 1967; Shoval et al., 2003). Furthermore, previous EXAFS measurements for diaspore concerned only Fe^{3+} (Hazemann et al., 1992) and not Cr^{3+}, in green single crystals of "Anatolian" diaspore (zultanite), formed in higher T, and occurred in diasporite at the Muğla metabauxite deposit of Turkey (e.g., Hatipoğlu et al., 2010).
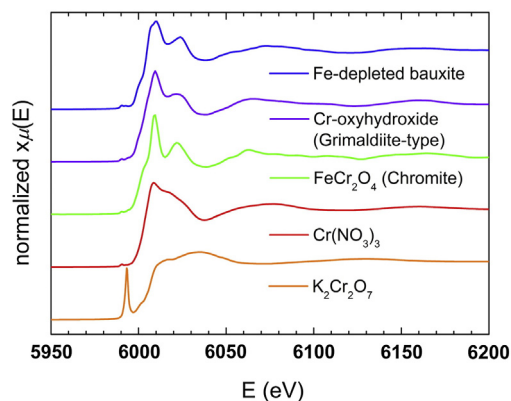

Fig. 7. Normalized Cr K-edge micro-XANES spectra with regard to Al-Fe-Cr-rich (diasporic) micro-areas of pisoliths (see Fig. 6) of high-grade Fe-depleted bauxite together with Cr reference materials. The diaspore spectrum (blue-colored line) is depicted with all references of Cr^{3+} (FeCr$_2$O$_4$/chromite: green-colored line; Cr(NO$_3$)$_3$/chromium nitrate: red-colored line), Cr^{6+} (K$_2$Cr$_2$O$_7$/potassium dichromate: orange-colored line) and grimaldiite-type material (Cr-oxyhydroxide: violet-colored line). (For interpretation of the references to colour in this figure legend, the reader is referred to the web version of this article.)
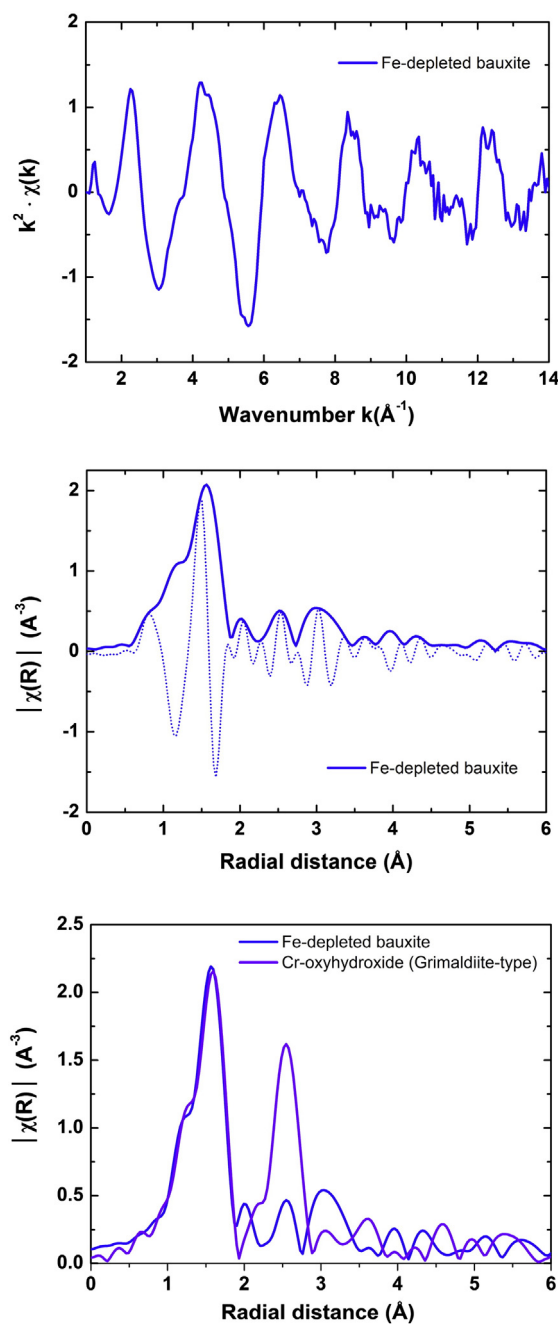

Fig. 8. Upper image: The Fourier transform (FT) of χ(k) of the Cr K-edge micro-EXAFS spectrum of diasporic pisoliths (see Fig. 6) of high-grade Fe-depleted bauxite (blue-colored line), using the ATHENA software (Ravel and Newville, 2005); middle image: The experimental FT plot in the magnitude part of χ(R) of the Cr K-edge EXAFS signal of the studied bauxite sample (blue-colored line), using the ATHENA software (Ravel and Newville, 2005); lower image: The experimental FT of χ(R) of the Cr K-edge EXAFS signal of the studied bauxite sample (blue-colored line) compared with the FT EXAFS signal of the Cr-oxyhydroxide (grimaldiite-type) reference material (violet-colored line), using the ATHENA software package (Ravel and Newville, 2005). (For interpretation of the references to colour in this figure legend, the reader is referred to the web version of this article.)

4.5. Mineralogical and chemical composition at the mesoscale and nanoscale

According to the SEM-STEM data, which enable us to investigate geological materials in the mesoscale, the studied bauxite consists of a diaspore matrix containing α-AlOOH grains with 500–2000 nm in size (i.e., apparent mesocrystals and microcrystals, see: Caraballo et al., 2015) rich in Ti (Fig. 10). Nevertheless, it is evident that Ti is still
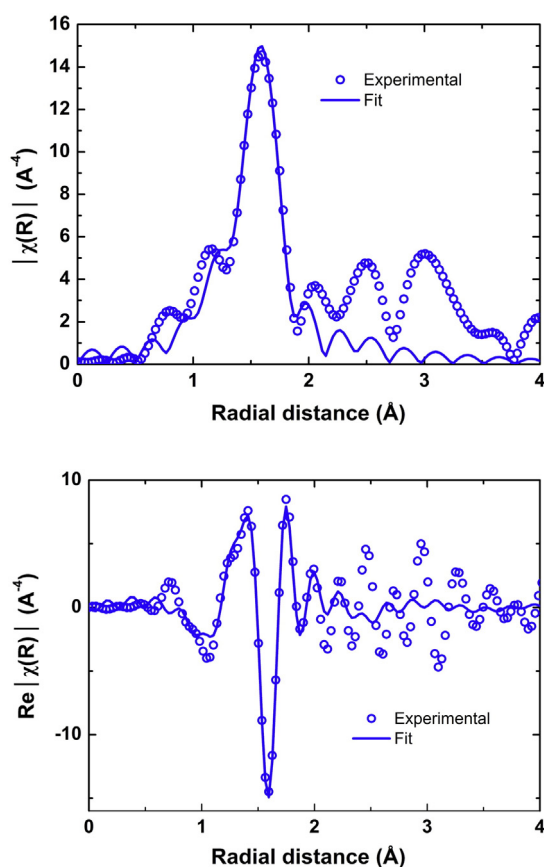
Fig. 9. The first shell, corresponding to Cr—O bond, EXAFS fit (Radial Distribution Function – RDF) plotted in $\chi(k)$ space (upper image), and also in the real part (lower image) of $\chi(R)$, using the ARTEMIS software package (Ravel and Newville, 2005).

distributed inhomogeneously, as also observed in the microscale by SEM-EDS (see Fig. 3). Thus, it is necessary for the nanoscale study of the bauxite, by TEM-EDS & EELS.

Bright-field (BF) images of the studied bauxite obtained by TEM, along with selected area electron diffraction (SAED) patterns, electron energy loss (EELS) spectra, TEM-EDS spectra and elemental maps, are presented in Figs. 11 and 12. To the best of our knowledge, this is the first detailed nanoscale study of AlOOH polymorphs in karst-type bauxite in literature, after the historical rough TEM images taken by Bárdossy and Mack (1967) and some data reported by Bárdossy and White (1979). In particular, the observed AlOOH polymorph at the nanoscale corresponds to diaspore (α-AlOOH). The viewing direction for the acquisition of its SAED pattern is [210] (see image a of Fig. 11). The EELS spectra obtained from the diaspore show signals of O (532 eV). A strong peak at 710 eV, corresponding to the Fe L_3 edge, is clearly observed (image c of Fig. 11). This spectrum is very similar to Fe^{3+}-containing Fe hydroxides and oxides, such as goethite and hematite (e.g., Chen et al., 2009). The results indicate that the valence of Fe in diaspore is 3+, and not 2+ appearing around 707–708 eV (e.g., Radtke et al., 2006). All EELS spectra from regions of diaspore, obtained with a beam size of ~10 nm, show the presence of Fe (see image c of Fig. 11), which was detected by SEM-EDS and [57]Fe Mössbauer spectroscopy. However, there are no detectable Fe nanoparticles in the above regions. The regions with brighter contrast appear to be pits or voids. Although the occurrence of both anatase and rutile was confirmed by PXRD (see Fig. 2), it was impossible to distinguish the two TiO_2 polymorphs at the microscale (see Fig. 3). As a consequence, the TEM-EDS & EELS study revealed relatively large, needle-like, rutile into the diaspore matrix with the viewing direction of its obtained SAED pattern at [113] (see image a of Fig. 11). On the other hand, anatase crystals are widely distributed into the diaspore matrix (see image b of Fig. 11), and have a rounded

shape with less than ca. 500 nm in size (i.e., mesocrystals and nanocrystals, see: Caraballo et al., 2015). The viewing direction of its SAED pattern is at [131]. Even though the structural characteristics of Ti and O atoms in both rutile and anatase - in terms of their nearest neighbor structural environment - are very similar, detectable differences can be observed between their EELS spectral data (see image d of Fig. 11). It is notable that EELS spectra, obtained from both the TiO_2 polymorphs, previously detected by SAED patterns, support the presence of a Ti-oxide phase without any Fe signal, in contrast to the case of ilmenites (e.g., Radtke et al., 2006). The characteristic features are in accordance with those observed in EELS spectra in literature (e.g., Brydson et al., 1989). In both TiO_2 polymorphs, the characteristic spin-orbit splitting of the L_3 and L_2 edges has been recorded in the obtained EELS spectra (see image d of Fig. 11). According to literature (e.g., Brydson et al., 1989), this can be attributed to the crystal-field splitting of the t_{2g} and e_g orbitals. However, there is a notable difference between the spin-orbit splitting that has been documented for rutile and anatase in the present study; this phenomenon is relatively less pronounced in the case of anatase. Moreover, additional spectral differences allow to distinguish rutile and anatase on the basis of: (i) the asymmetric peaks at 461 eV (Ti L_3 edge), (ii) the spacing between the peaks at 464 and 466 eV, which is smaller in anatase (~1.9 eV) than in rutile at 2.3 eV (Ti L_2 edge), and (iii) the shapes of the O K edges which are different between rutile and anatase EELS spectra and similar to those reported in literature (e.g., Brydson et al., 1989). Therefore, the TEM-EDS & EELS study confirms the absence of Fe—Ti oxides, and the presence of solely TiO_2 polymorphs, which do not contain Fe. Therefore, we could demonstrate that Ti mineral nanoparticles (Caraballo et al., 2015; Hochella, 2002a, 2002b; Hochella, 2006; Hochella, 2008; Hochella et al., 2012; Hochella et al., 2008; Plathe et al., 2010; Schindler and Hochella, 2016; Waychunas and Zhang, 2008) exist in the studied karst-type bauxite from Greece. In a relevant recent study, Gan et al. (2013) also reported TEM images of potential anatase grains (elemental maps in nanoscale and SAED patterns were not published) in the size 150–500 nm (mesocrystals), but not rutile, in karst-type bauxites from northern Europe. The co-existence of two TiO_2 polymorphs in bauxite raises questions about the origin of rutile. Rutile is usually formed in high-T and -P, so it is a common accessory mineral in metamorphic rocks (e.g., Goldsmith and Force, 1978) and is classified among the most stable detrital minerals in sedimentary systems (e.g., Zack et al., 2004). It may also be formed from the conversion of metastable anatase at low-P and 600 °C (Jamieson and Olinger, 1969). However, according to Bárdossy (1982), rutile in karst-type bauxites, except for the form of clastic (detrital) grains in the size between 10 and 200 μm, can also be low-T authigenic (diagenetic) and, rarely, epigenetic in μm-sized veins along with anatase. Anatase is a typically low-T authigenic phase, which can be syngenetic (to diaspore) and early diagenetic (Bárdossy, 1982). Contrary to anatase, it is obvious that the formation of rutile in low-T Al-ore deposits has remained questionable for a long time. However, it is known that the process of anatase transformation to rutile may take place in low-T at the nanoscale and, thus, there are particle size effects on transformation kinetics and phase stability in nanocrystalline TiO_2 (Gribb and Banfield, 1997; Smith et al., 2009; Zhou and Fichthorn, 2012). Taking into account all the above, we may also support the observations by Bárdossy (1982) and the "scale-effect" in bauxite minerals (Bárdossy, 2007) and, therefore, suggest that rutile can be authigenic - not-detrital - at the microscale and, definitely, at the nanoscale. In order to characterize Fe nanoparticles in diaspore, more than 15 regions were thoroughly studied via electron microscopy at the nanoscale, three of which were found to contain such materials. The precise phase identification was not feasible, because of aggregation with other phases, which make their lattice fringes totally invisible, or due to semi-amorphous/disordered or completely amorphous character. Thus, the TEM-EDS study revealed rounded Fe oxide nanoparticles between 25 and 43 nm in size (Fig. 12). These Fe-bearing nanoparticles may concern true nanocrystals in case they are
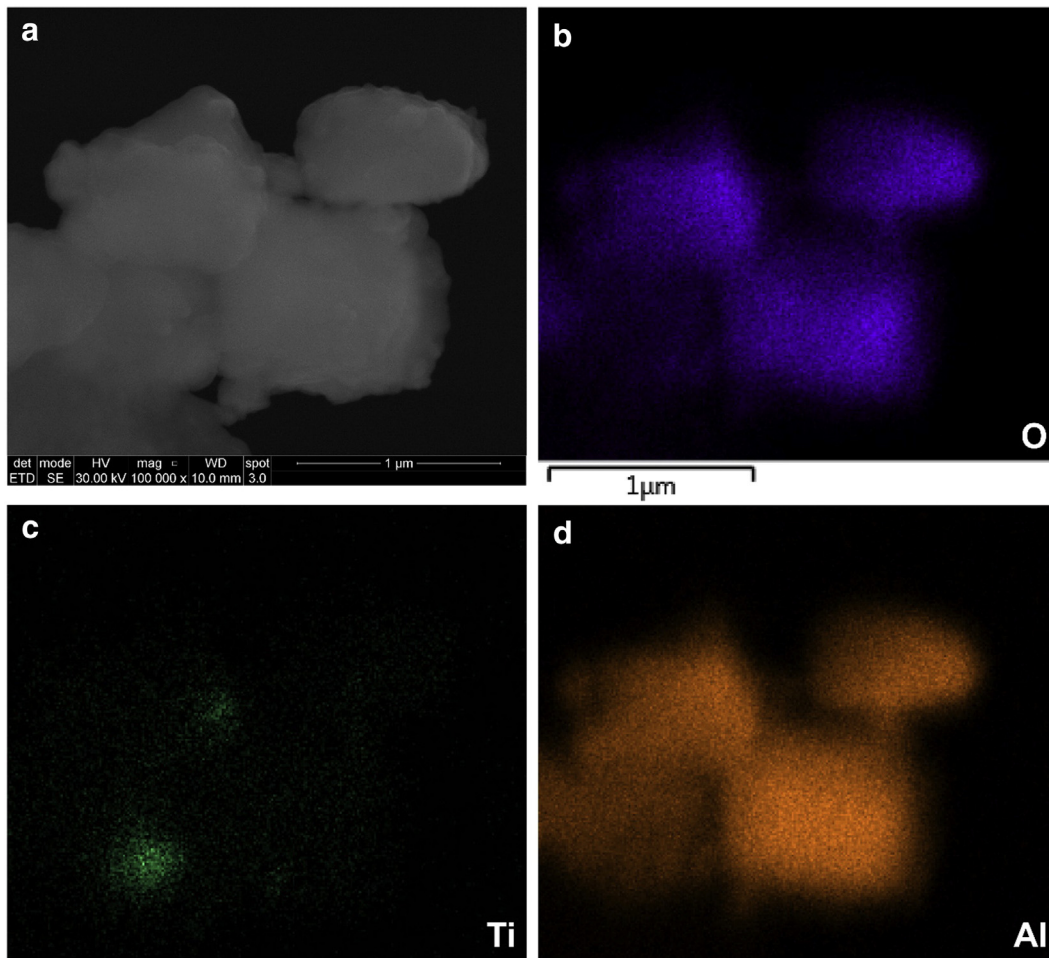
Fig. 10. Bright-field (BF) image (a) using STEM mode in the SEM QFEG that shows the distribution of Ti into the diaspore, as indicated by the relevant EDS elemental maps (b–d) at the mesoscale (Heaney, 2015; Caraballo et al., 2015).

crystalline nanomaterials (Caraballo et al., 2015). The EDS point analysis for a distinct Fe oxide particle with size 28 nm (see BF image and elemental map b of Fig. 12) clearly proved significant Fe (see left EDS spectrum image c of Fig. 12), while a region next to it did not comprise of Fe (see right EDS spectrum image c of Fig. 12). That confirms that the detected Fe signal comes from the nanoparticle and not from the TEM specimen holder or, even, from the pole-piece. The Cu signal is attributed to the TEM grid. The results prove that Fe in the studied bauxite is present in two forms, i.e. as Fe^{3+} ion in the diaspore structure and as Fe-oxide nanoparticles occluded in the diaspore matrix. The exact nature of these Fe-oxide nanoparticles is only partially clarified and, thus, it is difficult to claim whether they are counterparts of typical Fe minerals at the nanoscale. The evaluation of the ^{57}Fe Mössbauer spectra gave proof of the presence of maghemite, however not localized by the Laser micro-Raman and the electron microscopic techniques. Furthermore, the magnetic susceptibility measurements also provided evidence of the existence of maghemite. However, it is possible that precursor semi-amorphous/disordered Fe nanoparticles, such as ferrihydrite-type phases (e.g., Gilbert et al., 2013) or completely amorphous phases, can further undergo to crystalline Fe-oxide nanoparticles (e.g., Echigo et al., 2013), corresponding to maghemite. In another recent work, Gan et al. (2013) reported TEM images of Fe phases in karst-type bauxites, presumed to be typical crystalline mineral nanoparticles and, particularly, hematite 80 nm in size. Nevertheless, the Fe nanoparticles of the present study concern untypical Fe minerals in nanoscale, which can be described as Fe nanominerals, and can be crystalline, semi-amorphous/disordered and/or surface-disordered nanoparticles, amorphous-nanocrystalline transitional phases, or even completely

amorphous nanomaterials (Caraballo et al., 2015; Hochella, 2002a, 2002b; Hochella, 2006; Hochella, 2008; Hochella et al., 2012; Hochella et al., 2008; Plathe et al., 2010; Schindler and Hochella, 2016; Waychunas and Zhang, 2008).

4.6. Overview of the nano-mineralogy & -geochemistry and the role of nanogeoscience to the formation of high-grade diasporic karst-type bauxite

An overview of the nano-mineralogy and -geochemistry, revealed by a combination of spectroscopic and microscopic techniques, is graphically summarized in Fig. 13. The observed Fe nanominerals and Ti mineral nanoparticles also seem to play a vital role in the overall bauxitization processes and the formation of the studied high-grade (Fe-depleted) diasporic karst-type bauxite in Parnassos-Ghiona deposits (Fig. 1).

In principle, the bauxitization processes, starting from the supergene alteration of primary aluminosilicate minerals and the precipitation of amorphous (colloidal) Al- & Fe-hydroxides and silica, are followed by the enrichment of alumina through the abstraction of silica and the depletion of mobile elements, such as Na, K, and Ca (Pohl, 2011). Further aging (diagenesis) transforms the amorphous phases into stable oxyhydroxide/oxide minerals of Al, Ti and Fe, in various scales, and consolidates the original aluminous material into solid bauxite ore. However, regarding the allochthonous karst-type bauxites, bauxitization is rather complicated, in contrast to the simpler in-situ laterization processes related to lateritic (so-called "tropical") bauxites (Bárdossy and Aleva, 1990). In addition, most karstic bauxites have an ordinary lateritic bauxite origin and are essentially detrital bauxite sediments, after
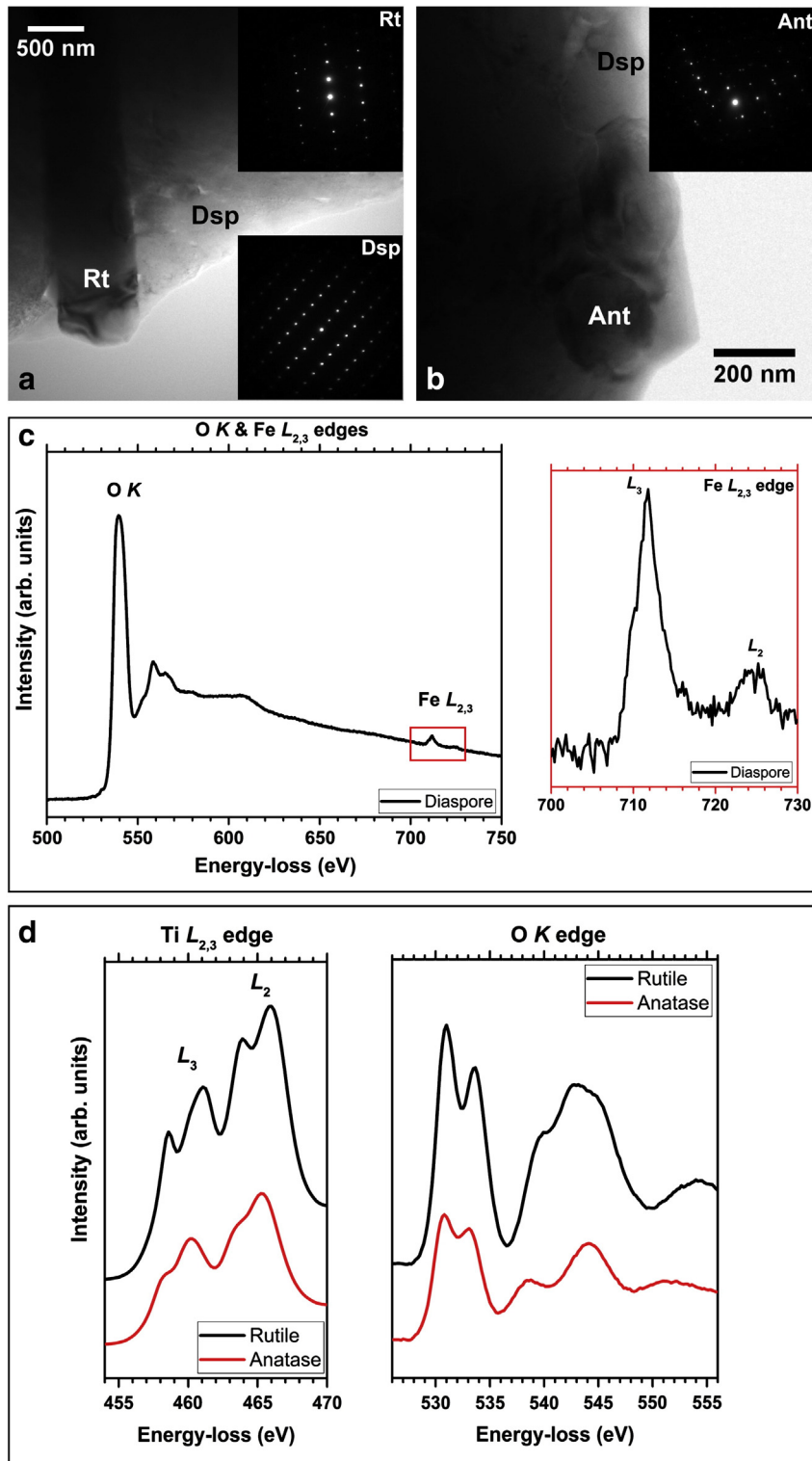
Fig. 11. TEM data for Ti mineral nanoparticles (TiO_2 polymorphs) occluded into the diaspore of the high-grade karst-type bauxite. BF images and SAED patterns for diaspore (a: the viewing direction for SAED pattern is [210]), rutile (a: the viewing direction for SAED pattern is [113]) and anatase (b: the viewing direction for SAED pattern is [131]; the pattern is a bit off from the zone axis). The recorded EELS spectra of O K edge (c) and Fe $L_{2,3}$ edge (enlarged view of the focused area with red-colored rectangle) in diaspore as well as the EELS of Ti $L_{2,3}$ edge in rutile and anatase (d) are illustrated after background subtraction and deconvolution. (For interpretation of the references to colour in this figure legend, the reader is referred to the web version of this article.)

erosion and transport (Pohl, 2011). Particularly, karst bauxites in the so-called Mediterranean belt (Bárdossy, 1982; Valeton, 1972; Özlü, 1983), including parts of central Europe, the Balkans and Middle East/Western Asia, are fundamentally hosted in Mesozoic marine sedimentary carbonate rocks, limestones, derived from the Tethys paleo-Ocean.

Seasonal climatic variations are also considered important to the formation of bauxitic ores as the alternation of wet and dry spells promotes fluctuations in groundwater levels and, hence, dissolution and mass transfer. Thus, most of the bauxite deposits are ordered after their age, according to alignments indicating the existence of palaeoclimatic
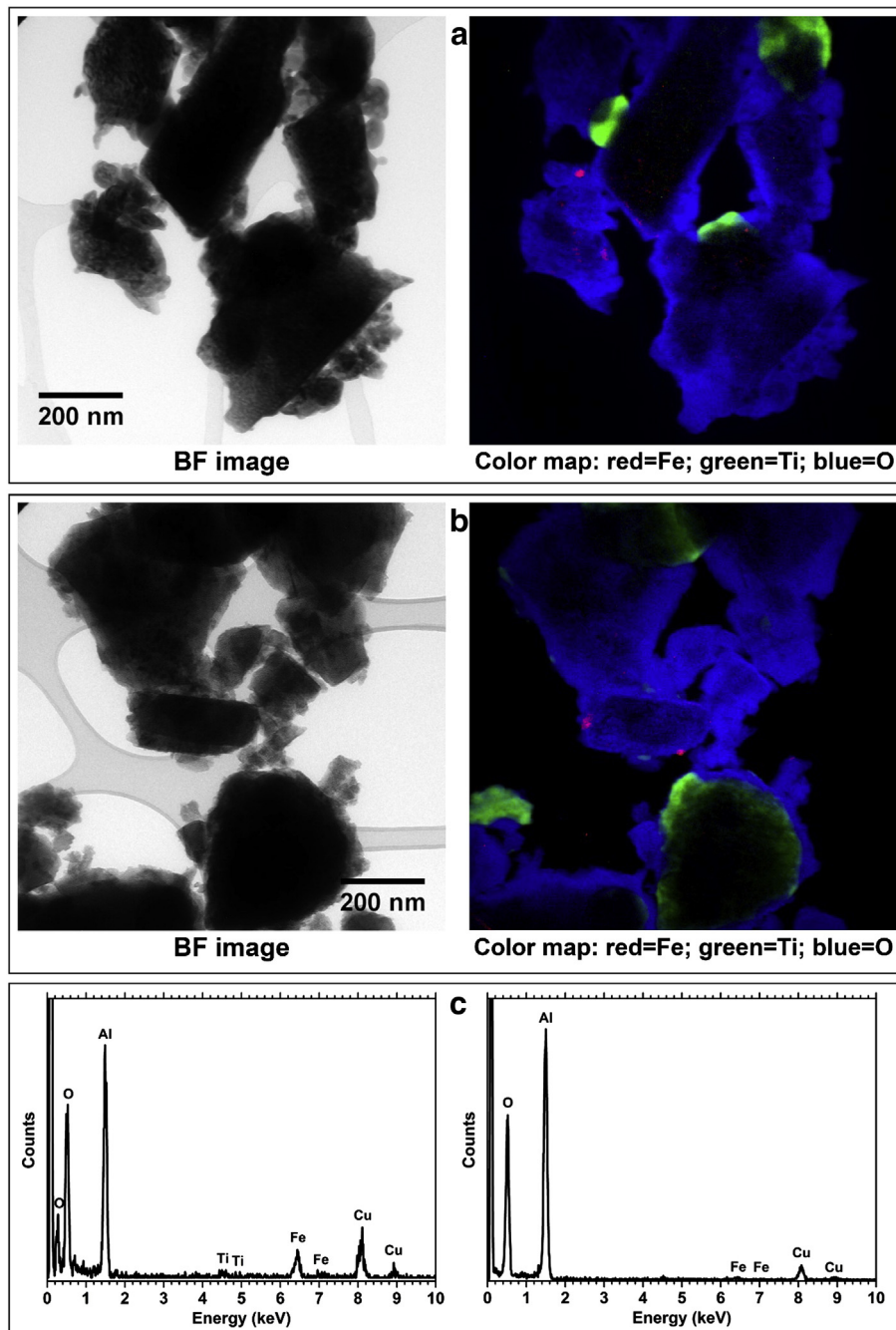
Fig. 12. Upper and middle images a & b: TEM-EDS data of Fe nanominerals, together with TiO$_2$ mineral nanoparticles into the diaspore of high-grade karst-type bauxite, with 25 nm in size (Fe elemental map of image a), with 28 nm in size (right nanoparticle at Fe elemental map of image b) and with 43 nm in size (left nanoparticle at Fe elemental map of image b), respectively. The latter Fe nanoparticle is clearly on diaspore. Any other contrast in the Fe elemental map of images a and b is due to artefacts attributed to diffraction contrast variation during the acquisition. Lower image c: A representative TEM-EDS point analysis obtained at a Fe nanoparticle (elemental map of image b) containing significant Fe amount (left EDS spectrum of image c), while a region next to it does not contain any detectable Fe content (right EDS spectrum of image c).

belts of humid intertropical type that were susceptible to having generated a laterizing pedogenesis, during geological time when these bauxites and laterites were formed (Nicolas and Bildgen, 1979; Robb, 2005). Subsequently, special climatic periods during Earth's history along with the greenhouse effect, allowed intense lateritic weathering during limited time intervals and, therefore, the formation of bauxite deposits (Bárdossy and Aleva, 1990; Valeton, 1994). Among various weathering periods that have been recorded in the European continent during the Late Mesozoic era and Tertiary period, the Upper Jurassic to Eocene epoch, and particularly the Cretaceous interval, is considered the most important for bauxitization processes (Bárdossy, 1982). The Cretaceous

period is generally considered to have been a time of typically warm climate. Moreover, Steuber et al. (2005) studied rudist bivalves (Hippuritoidea) to record intra-shell variations in $\delta^{18}O$ values and hence the evolution of the seasonality of Cretaceous sea surface temperatures. The study indicated high maximum temperatures ($\sim$35 to 37 °C) and relatively low seasonal variability (<12 °C) between 20° and 30° N during the warmer episodes. It is evident that Cretaceous seas of the Tethys paleo-Ocean were exceptionally warm (between 6 and 14 °C warmer than today) and the growth of rudists, as major reef building organisms, was favored in carbonate platforms (Skelton et al., 2006). During this geological period, rudist reefs were so dominant that they
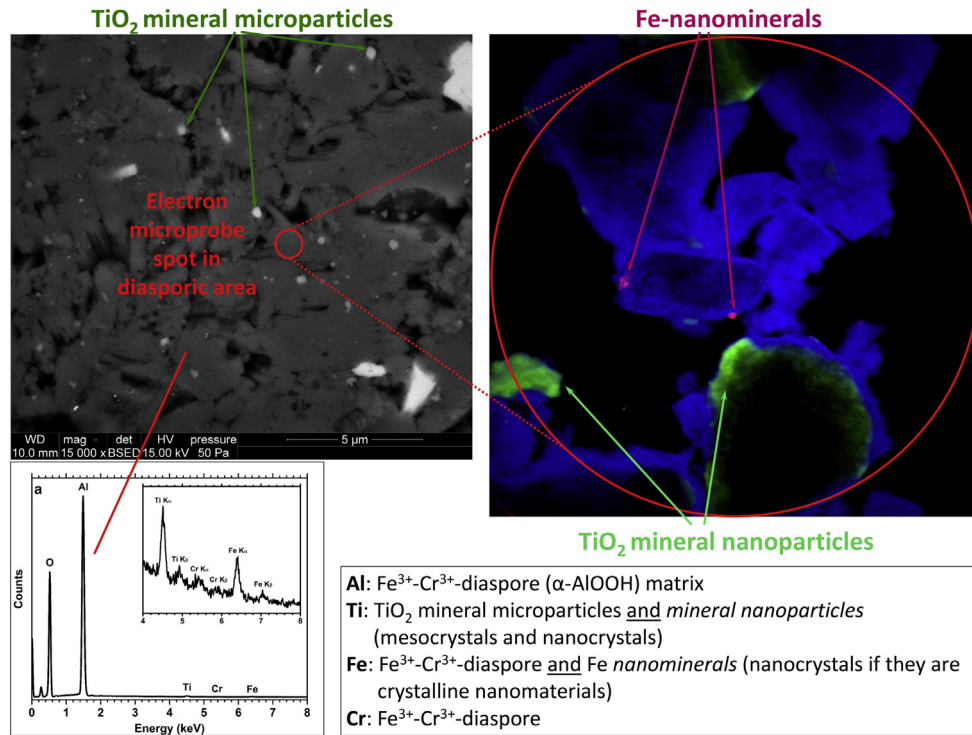
Fig. 13. Overview of the nano-mineralogy and -geochemistry of high-grade diasporic karst-type bauxite from Parnassos-Ghiona mines, Greece, based on a combination of spectroscopic (Laser micro-Raman, Mössbauer & magnetic susceptibility, SR micro-XRF, micro-XANES/-EXAFS), electron microscopic data at the microscale (SEM-EDS), the mesoscale (SEM-STEM) and at the nanoscale (TEM-EDS & EELS; for scale bar see Fig. 12).

pushed scleractinian corals out of many tropical environments, including shelves that occur in the Caribbean and Mediterranean during the current time. In general, Cretaceous, apart from the characteristic warm climate, is characterized by low atmospheric O_2, and in parallel by high CO_2, related to severe greenhouse effect (Berner, 1999; Royer, 2006). This also stands for Upper Jurassic, implying that atmospheric and climate conditions in the entire period of Upper Jurassic–Upper Cretaceous promoted the intense lateritic weathering and bauxitization processes. It is also evident that the paleogeography plays an important role in the formation of karst-type bauxites. Valeton (1994) has reported a model for the paleogeographic situation in central Greece during neighboring Ni-laterite deposits evolution on ophiolites and bauxite formation on laterite-derived facies covering the carbonate platform of the foreland. In the Mesozoic coastal area, from the land to the seaward side in several sequences, bauxite events are each related to a transgressive phase. In particular, short-lived emergence episodes due to regression of the sea interrupted the marine sedimentation, resulting in exposure of the carbonate platform to freshwater alteration and the development of karst. Bauxitic material, which derived from the erosion of lateritic bauxites exposed in the adjacent Pelagonian geotectonic zone, was subsequently transported and deposited into the karst. The bauxite formation (bauxitization) is related to the coastal areas and to the times where transgression began. During three periods of regression and an uplift of the terrestrial hinterland, the laterites on ophiolites and surrounding rocks were reworked in the northeast and deposited as "laterite-derived facies" (LDF) in the southwest. Due to the rise of the ground-water level during the subsequent transgression, the LDF was transformed into bauxite. It is also believed that degradation of lateritic weathering crusts resulted in the deposition of bauxitic material such as talus and colluvium on the slopes, followed by reworking and transport by river systems. Further diagenesis resulted in (i) leaching of silica and Fe under partly reducing conditions, and (ii) re-crystallization of Fe minerals and crystal growth of AlOOH (diaspore and/or boehmite) and TiO_2 (anatase and rutile) authigenic polymorphs. Additional intense

supergene/epigenetic processes (epigenesis) caused re-distribution of more mobile elements like Fe, Mn, Ba and Zn, which were precipitated, commonly as black crusts, in traps near the karstified footwall limestone. The Fe minerals species and their location indicate several phases of Fe mobilization, (i) the first Fe mobilization and re-precipitation as hematite is contemporaneous with the crystallization of diaspore, (ii) a subsequent second mobilization of Fe under reducing and stagnating groundwater conditions resulted in the growth of Fe sulfides (pyrite), which is followed by (iii) a final epigenetic Fe migration/epigenetic Fe bleaching related, most likely, to the formation of Fe-depleted bauxite in the topmost part of the B3 horizon (Valeton et al., 1987; Valeton, 1994; see Fig. 1). Thus, according to Valeton (1972), the bauxitization processes, after the initial deposition of weathered/residual material in pre-existing karst cavities, concern diagenesis, epigenesis and, occasionally, younger weathering, causing Al, Fe and Ti to be displaced several times. Moreover, as far as the case of the samples studied in the present work is concerned, it has been reported that the deposition of a coal layer lying unconformably over the B3 bauxite horizon, and covered by the Turonian–Senonian bituminous (dark colored) hanging-wall limestone, took place in a paralic sedimentary environment; this was characterized by rheotrophic, high groundwater table (lacustrine) conditions for the peat forming stage except the uppermost part, which was affected by oxidizing conditions. The karst cavities of the footwall limestone, filled with bauxite during a period of sea regression, were suitable sites for the formation of lagoons, possibly behind barrier bars formed on the shallow carbonate platform. Oxidation of the upper part of the pyrite-rich coal might have resulted in bleaching of the bauxite by downwards penetrating acidic ($SO_4^=$-containing) solutions. The oxidation was probably caused syngenetically on the palaeomire surface by the wave action of the transgressing sea or epigenetically in the coal layer by the drainage of waters. Either one or both of the above effects may explain the contribution of coal to the formation of high-grade Fe-depleted bauxite (Kalaitzidis et al., 2010). According to other authors, the driving force, for formation of this type of bauxites,

could be micro-organisms involved in biomineralization processes (Laskou and Economou-Eliopoulos, 2013; Laskou and Economou-Eliopoulos, 2007; Laskou et al., 2011).

Nevertheless, Bárdossy and White (1979) mentioned that acidic solutions dissolve most of the Fe minerals and, occasionally, part of the Al minerals. However, there is no proof of the dissolution and re-precipitation of Ti minerals. Moreover, there are no previous reports about the chemical behavior of Cr. Taking into account all the above and the results of the present study, we consider that Fe^{3+}-Cr^{3+}-diaspore is formed during the diagenesis, most probably, together with TiO_2 mineral microparticles and mineral nanoparticles (see Fig. 13). We consider that these phases remain rather stable during epigenesis and, only, partial elemental mobility (mostly Fe) can take place. The high immobility of Ti-oxides in nature is well known (e.g., Nesbitt, 1979), whereas Ti, Zr, Nb, Ga and Th are the most immobile elements in bauxites (Pohl, 2011). It is herein worthy to note that Nb and Th in the studied bauxite samples are subsequently associated with TiO_2 (anatase) phases (Gamaletsos, 2014; Gamaletsos et al., 2011). On the other hand, mixed Al-Fe-(Cr)-oxides are metastable compounds that can persist for prolonged geological time due to small energy differences between the stable and metastable phases (Mazlan and Navrotsky, 2003). In contrast, the observed Fe nanominerals may be associated with supergene/epigenetic processes. It is, therefore, implied that Fe depletion, attributed to percolating acidic solutions and/or micro-organisms, simultaneously leading to the formation of high-grade bauxite, is associated with intense geological nano-scale processes, related to continuous karstification. Finally, we consider that younger weathering processes have minimal effect on the TiO_2 mineral nanoparticles and the Fe nanominerals, although the precipitation of secondary Fe-Al-sulfate phases (Laskou et al., 2011) could be attributed to an additional Fe mobility from Fe-Cr-diaspore (and, also, S mobility from overlying sulfide-rich coal and bauxite enclaves).

5. Conclusions

The main conclusions, concerning the nano-mineralogy and -geochemistry of high-grade diasporic karst-type bauxite, from Parnassos-Ghiona mines (Greece), are summarized below:

- The main crystalline mineralogical phase, formed during diagenesis, and comprising -in fact- the Al-matrix of the ore, is a novel type of Fe-Cr-diaspore specifically a Fe^{3+}-Cr^{3+}-AlOOH (α-AlOOH), where $^{[6]}Fe^{3+}$ and $^{[6]}Cr^{3+}$ substitute for $^{[6]}Al^{3+}$ in the α-AlOOH structure.
- Apart from Al, Fe and Cr, Ti is also a major metal in the ore, occurring in the form of TiO_2 polymorphs (anatase and rutile), also formed during diagenesis, which are detectable in microscale as well as in nanoscale in the form of Ti mineral nanoparticles.
- In the case of Fe, apart from Fe^{3+} ions in the diaspore, there are also Fe oxide nanominerals, formed during epigenesis, exhibiting most likely a maghemite-type composition.
- The Ti mineral nanoparticles and Fe nanominerals occluded into the Fe-Cr-diaspore, and described for the first time in literature with regard to karst-type bauxite deposits, illustrate the importance of nano-mineralogy, nano-geochemistry and, in general, of nanogeoscience, in the exploration and exploitation of major Al mineral resources of the world.

Finally, the present study gives corroborative evidence of the importance of nanogeoscience in the characterization of Al-ores and, in general, of metal oxide/hydroxide ore deposits, as it has been proven in the case of metals in sulfide ores. Mineral nanoparticles and nanominerals may be considered the final frontier of ore mineralogy and geochemistry, playing a vital role ore in the exploration and exploitation of basic, noble and strategic metal resources.

References

Aragón, R., Buttrey, D., Shepherd, J., Honig, J., 1985. Influence of nonstoichiometry on the Verwey transition. Phys. Rev. B 31, 430–436.

Arp, T., 1985. Geologische Kartierung des Gebietes um Tithronion im Kallidromongebirge, Mittelgriechenland und petrographische Bearbeitung des Karstbauxites (b1). Unpublished Ph.D thesis. University of Hamburg, Hamburg, Germany (213pp).

Bárdossy, G., 1982. Karst Bauxites: Bauxite Deposits on Carbonate Rocks: Developments in Economic Geology 14. Elsevier, Amsterdam (441 pp.).

Bárdossy, G., 2007. The Halimba bauxite deposit. In: Maros, G. (Ed.), Occasional Papers of the Geological Institute of Hungary Vol. 208. Geological Institute of Hungary, p. 119.

Bárdossy, G., Aleva, G.J.J., 1990. Lateritic Bauxites: Development in Economic Geology27. Elsevier, Amsterdam (624 pp.).

Bárdossy, G., Mack, E., 1967. Zur kenntnis der bauxite des Parnass-Kiona-Gebirges. Mineral. Deposita 2, 334–348.

Bárdossy, G., White, J.L., 1979. Carbonate inhibits the crystallization of aluminum hydroxide in bauxite. Science 203, 355–356.

Barker, S.L.L., Hickey, K.A., Cline, J.S., Dipple, G.M., Kilburn, M.R., Vaughan, J.R., Longo, A.A., 2009. Uncloaking invisible gold: use of nanosims to evaluate gold, trace elements, and sulfur isotopes in pyrite from Carlin-type gold deposits. Econ. Geol. 104, 897–904.

Berner, R.A., 1999. Atmospheric oxygen over Phanerozoic time. Proc. Natl. Acad. Sci. U. S. A. 96, 10955–10957.

Biermann, M., 1983. Zur mineralogie, geochemie und genese des karstbauxites (B3 – horizont) an der Grenze Unter-Oberkreide in Mittelgriechenland. Unpublished Ph.D thesis. University of Hamburg, Hamburg, Germany (134 p).

Brydson, R., Sauer, H., Engel, W., Thomass, J.M., Zeitler, E., Kosugi, N., Kuroda, H., 1989. Electron energy loss and X-ray absorption spectroscopy of rutile and anatase: a test of structural sensitivity. J. Phys. Condens. Matter 1, 797–812.

Busing, W.R., Levy, H.A., 1958. A single crystal neutron diffraction study of diaspore, AlO(OH). Acta Crystallogr. 11, 798–803.

Caraballo, M.A., Michel, F.M., Hochella Jr., M.F., 2015. The rapid expansion of environmental mineralogy in unconventional ways: beyond the accepted definition of a mineral, the latest technology, and using nature as our guide. Am. Mineral. 100, 14–25.

Chen, S.-Y., Gloter, A., Zobelli, A., Wang, L., Chen, C.-H., Colliex, C., 2009. Electron energy loss spectroscopy and *ab initio* investigation of iron oxide nanomaterials grown by a hydrothermal process. Phys. Rev. B 79 (104103), 1–10.

Christensen, A.N., Hansen, P., Lehmann, M.S., 1976. Isotope effects in the bonds of beta-CrOOH and beta-CrOOD. J. Solid State Chem. 19, 299–304.

Christensen, A.N., Hansen, P., Lehmann, M.S., 1977. Isotope effects in the bonds of α-CrOOH and α-CrOOD. J. Solid State Chem. 21, 325–329.

Ciobanu, C.L., Cook, N.J., Utsunomiya, S., Pring, A., Green, L., 2011. Focused ion beam-transmission electron microscopy applications in ore mineralogy: bridging micro- and nanoscale observations. Ore Geol. Rev. 42, 6–31.

Ciobanu, C.L., Cook, N.J., Utsunomiya, S., Kogagwa, M., Green, L, Gilbert, S., Wade, B., 2012. Gold-telluride nanoparticles revealed in arsenic-free pyrite. Am. Mineral. 97, 1515–1518.

Ciobanu, C.L., Cook, N.J., Wade, B.P., Ehrig, K., 2014. Ore minerals down to nanoscale: petrogenetic implications. Acta Geol. Sin. (Engl. Ed.) 88, 1441–1443.

Cornell, R.M., Schwertmann, U., 2003. The Iron Oxides: Structure, Properties, Reactions, Occurrences and Uses. Wiley-VCH Verlag GmbH & Co. KGaA (664 pp.).

Cosmidis, J., Benzerara, K., Gheerbrant, E., Estève, I., Bouya, B., Amaghzaz, M., 2013. Nanometer-scale characterization of exceptionally preserved bacterial fossils in Paleocene phosphorites from Ouled Abdoun (Morocco). Geobiology 11, 139–153.

Cromer, D.T., Herrington, K., 1955. The structures of anatase and rutile. J. Am. Chem. Soc. 77, 4708–4709.

Culltity, B.D., Graham, C.D., 2009. Introduction to Magnetic Materials. second ed. Wiley.

Deditius, A.P., Utsunomiya, S., Reich, M., Kesler, S.E., Ewing, R.E., Hough, R., Walshe, J., 2011. Trace metal nanoparticles in pyrite. Ore Geol. Rev. 42, 32–46.

Douvalis, A.P., Polymeros, A., Bakas, T., 2010. A ^{57}Fe–^{119}Sn Mössbauer spectra computer fitting program with novel interactive user interface. J. Phys. Conf. Ser. 217 (012014), 1–4.

Douvallet, L., Martin, F., Soubiès, F., Salvi, S., Melfi, A.J., Fortuné, J.P., 1999. The mobility of zirconium and identification of secondary Zr-bearing phases in bauxite from Poços de Caldas, Minas Gerais, Brazil. A mass-balance and X-ray absorption spectroscopic study. Can. Mineral. 37, 635–651.

Dyar, M.D., Agresti, D.G., Schaefer, M.W., Grant, C.A., Sklute, E.C., 2006. Mössbauer spectroscopy of earth and planetary materials. Annu. Rev. Earth Planet. Sci. 34, 83–125.

Echigo, T., Monsegue, N., Aruguete, D.M., Murayama, M., Hochella Jr., M.F., 2013. Nanopores in hematite (α-Fe_2O_3) nanocrystals observed by electron tomography. Am. Mineral. 98, 154–162.

EU Ad-hoc Working Group, 2014. Report on critical raw materials for the EU. Report of the Ad Hoc Working Group on Defining Critical Raw Materials (http://ec.europa.eu/growth/sectors/raw-materials/specific-interest/critical/index_en.htm).

Filimonova, L.G., Trubkin, N., 2008. Micro- and nanoparticles of zincite and native zinc from disseminated mineralization of metasomatic rocks in the Dukat ore field. Geol. Ore Deposits 50, 153–163.

Fougerouse, D., Reddy, S.M., Saxey, D.W., Richard, W.D.A., Riessen, A.V., Micklethwaite, S., 2016. Nanoscale gold clusters in arsenopyrite controlled by growth rate not concentration: evidence from atom probe microscopy. Am. Mineral. 101, 1916–1919.

Francombe, M.H., 1957. Lattice changes in spinel-type iron chromites. J. Phys. Chem. Solids 3, 37–43.

Fysh, S.A., Clark, P.E., 1983. A Mössbauer study of the iron mineralogy of acid-leached bauxite. Hydrometallurgy 10, 285–303.

Gamaletsos, P., 2014. Mineralogy and Geochemistry of Bauxites From Parnassos-Ghiona Mines and the Impact on the Origin of the Deposits. Unpublished PhD Thesis. National and Kapodistrian University of Athens (361pp).

Gamaletsos, P., Godelitsas, A., Chatzitheodoridis, E., Kostopoulos, D., 2007. Laser micro-Raman investigation of Greek bauxites from the Parnassos-Ghiona active mining area. Bull. Geol. Soc. Greece 40, 736–746.

Gamaletsos, P., Godelitsas, A., Mertzimekis, T.J., Göttlicher, J., Steininger, R., Xanthos, S., Berndt, J., Klemme, S., Kuzmin, A., Bárdossy, G., 2011. Thorium partitioning in Greek industrial bauxite investigated by synchrotron radiation and laser-ablation techniques. Nucl. Inst. Methods Phys. Res. B 269, 3067–3073.

Gamaletsos, P.N., Godelitsas, A., Kasama, T., Kuzmin, A., Lagos, M., Mertzimekis, T.J., Göttlicher, J., Steininger, R., Xanthos, S., Pontikes, Y., Angelopoulos, G.N., Zarkadas, C., Komelkov, A., Tzamos, E., Filippidis, A., 2016. The role of nano-perovskite in the negligible thorium release in seawater from Greek bauxite residue (red mud). Sci. Rep. 6 (21737), 1–13.

Gan, B.K., Taylor, Z., Xu, B., Van Riessen, A., Hart, R.D., Wang, X., Smith, P., 2013. Quantitative phase analysis of bauxites and their dissolution products. Int. J. Miner. Process. 123, 64–72.

Gendler, T.S., Shcherbakov, V.P., Dekkers, M.J., Gapeev, A.K., Gribov, S.K., McClelland, E., 2005. The lepidocrocite-maghemite-haematite reaction chain-I. Acquisition of chemical remanent magnetization by maghemite, its magnetic properties and thermal stability. Geophys. J. Int. 160, 815–832.

Geological Survey, U.S., 2015. Bauxite and aluminae. Stat. Inf. (http://minerals.usgs.gov/minerals/pubs/commodity/bauxite).

Gilbert, B., Erbs, J.J., Lee Penn, R., Petkov, V., Spagnoli, D., Waychunas, G.A., 2013. A disordered nanoparticle model for 6-line ferrihydrite. Am. Mineral. 98, 1465–1476.

Goldsmith, R., Force, E.R., 1978. Distribution of rutile in metamorphic rocks and implications for placer deposits. Mineral. Deposita 13, 329–343.

Gribb, A.A., Banfield, J.F., 1997. Particle size effects on transformation kinetics and phase stability in nanocrystalline TiO_2. Am. Mineral. 82, 717–728.

Hatipoğlu, M., Helvacı, C., Chamberlain, S.C., Babalık, H., 2010. Mineralogical characteristics of unusual "Anatolian" diaspore (zultanite) crystals from the İlbirdağı diasporite deposit, Turkey. J. Afr. Earth Sci. 57, 525–541.

Hazemann, J.L., Bérar, J.F., Manceau, A., 1991. Rietveld studies of the aluminium-iron substitution in synthetic goethite. Mater. Sci. Forum 79, 821–826.

Hazemann, J.L., Manceau, A., Sainctavit, P., Malgrange, C., 1992. Structure of the $\alpha Fe_xAl_{1-x}OOH$ solid solution. Phys. Chem. Miner. 19, 25–38.

Heaney, P.J., 2015. At the blurry edge of mineralogy. Am. Mineral. 100, 3.

Helmy, H.M., Ballhaus, C., Fonseca, R.O.C., Wirth, R., Nagel, T., Treboux, M., 2013. Noble metal nanoclusters and nanoparticles precede mineral formation in magmatic sulphide melts. Nat. Commun. 4, 1–7.

Hill, R.J., 1979. Crystal structure refinement and electron density distribution in diaspore. Phys. Chem. Miner. 5, 179–200.

Hill, V.G., Weir, C., Collins, R.L., Hoch, D., Radcliffe, D., Wynter, C., 1978. Application of Mössbauer spectroscopy to iron-57 bauxite. Hyperfine Interact. 4, 444–447.

Hochella Jr., M.F., 2002a. There's plenty of room at the bottom: nanoscience in geochemistry. Geochim. Cosmochim. Acta 66, 735–743.

Hochella Jr., M.F., 2002b. Nanoscience and technology: the next revolution in the Earth sciences. Earth Planet. Sci. Lett. 203, 593–605.

Hochella Jr., M.F., 2006. The case of nanogeoscience. Ann. N. Y. Acad. Sci. 1093, 108–122.

Hochella Jr., M.F., 2008. Nanogeoscience: from origin to cutting-edge applications. Elements 4, 373–379.

Hochella Jr., M.F., Lower, S.K., Maurice, P.A., Penn, R.L., Sahai, N., Sparks, D.L., Twining, B.S., 2008. Nanominerals, mineral nanoparticles, and earth systems. Science 319, 1631–1635.

Hochella Jr., M.F., Aruguete, D., Kim, B., Madden, A.S., 2012. Naturally occurring inorganic nanoparticles: general assessment and a global budget for one of Earth's last unexplored geochemical components. In: Barnard, A.S., Guo, H. (Eds.), Nature's Nanostructures. Pan Stanford Publishing, Australia, pp. 1–42.

Hough, R.M., Noble, R.R.P., 2010. Colloidal gold nanoparticles in ore systems. Abstracts of Goldschmidt Conference, Knoxville, Tennessee, USA Vol. 2010, p. A420.

Hough, R.M., Noble, R.R.P., Hitchen, G.J., Hart, R., Reddy, S.M., Saunders, M., Clode, P., Vaughan, D., Lowe, J., Gray, D.J., Anand, R.R., Butt, C.R.M., Verrall, M., 2008. Naturally occurring gold nanoparticles and nanoplates. Geology 36, 571–574.

Hough, R.M., Noble, R.R.P., Reich, M., 2011. Natural gold nanoparticles. Ore Geol. Rev. 42, 55–61.

Hough, R., Reich, M., Noble, R., 2012. Noble metal nanoparticles in ore systems. In: Barnard, A.S., Guo, H. (Eds.), Nature's Nanostructures. Nature's nanostructures: Pan Stanford Publishing, Australia, pp. 141–168.

Howard, C.J., Sabine, T.M., Dickson, F., 1991. Structural and thermal parameters for rutile and anatase. Acta Crystallogr. B B47, 462–468.

Hummer, D.R., Heaney, P.J., Post, J.E., 2007. Thermal expansion of anatase and rutile between 300 and 575 K using synchrotron powder X-ray diffraction. Powder Diffract. 22, 352–357.

Jamieson, J.C., Olinger, B., 1969. Pressure-temperature studies anatase, brookite, rutile, and TiO_2 (II): a discussion. Am. Mineral. 54, 1477–1481.

Kakol, Z., Sabol, J., Stickler, J., Honig, J., 1992. Effect of low-level titanium (IV) doping on the resistivity of magnetite near the Verwey transition. Phys. Rev. B 46, 1975–1978.

Kalaitzidis, S., Siavalas, G., Skarpelis, N., Araujo, C.V., Christanis, K., 2010. Late Cretaceous coal overlying karstic bauxite deposits in the Parnassus-Ghiona unit, Central Greece: coal characteristics and depositional environment. Int. J. Coal Geol. 81, 211–226.

Klug, A., Farkas, L., 1981. Structural investigations of polycrystalline diaspore samples by X-ray powder diffraction. Phys. Chem. Miner. 7, 138–140.

Koneev, R.I., Khalmatov, R.A., Mun, Y.S., 2010. Nanomineralogy and nanogeochemistry of ores from gold deposits of Uzbekistan. Geol. Ore Deposits 52, 755–766.

Kotova, O., Gasaleeva, G., Vakhrushev, A., 2015. Minerals of bauxites and residues: problems of processing and enrichment (Russia). Proceedings of the 11th International Congress for Applied Mineralogy (ICAM). Springer, pp. 241–251.

Kuzmann, E., Nagy, S., Vértes, A., 2003. Critical review of analytical applications of Mössbauer spectroscopy illustrated by mineralogical and geological examples (IUPAC technical report). Pure Appl. Chem. 75, 801–858.

Larson, A.C., Von Dreele, R.B., 2004. General structure analysis system (GSAS). Los Alamos National Laboratory Report, LAUR, pp. 86–748.

Laskou, M., Economou-Eliopoulos, M., 2007. The role of microorganisms on the mineralogical and geochemical characteristics of the Parnassos-Ghiona bauxite deposits, Greece. J. Geochem. Explor. 93, 67–77.

Laskou, M., Economou-Eliopoulos, M., 2013. Bio-mineralization and potential biogeochemical processes in bauxite deposits: genetic and ore quality significance. Mineral. Petrol. 107, 471–486.

Laskou, M., Economou-Eliopoulos, M., Mitsis, I., 2011. Bauxite ore as an energy source for bacteria driving iron-leaching and bio- mineralization. Hellenic J. Geosci. 45, 163–173.

Mazlan, J., Navrotsky, A., 2003. Thermodynamics of the goethite-diaspore solid solution. Eur. J. Mineral. 15, 495–501.

Meil'man, M.L., Torchinskii, I.A., 1967. Isomorphism of chromium in diaspore. J. Struct. Chem. 7 (4), 578–579.

Mondillo, N., Nieto, F., Balassone, G., 2015. Micro- and nano-characterization of Zn-clays in nonsulfide supergene ores of southern Peru. Am. Mineral. 100, 2484–2496.

Morin, F.J., 1950. Magnetic susceptibility of α-Fe_2O_3 and α-Fe_2O_3 with added titanium. Phys. Rev. 78, 819–820.

Murad, E., 2005. Characterization of a standard bauxite and its deferration products by Mössbauer spectroscopy. Miner. Eng. 18, 984–986.

Muxworthy, A.R., 1999. Low-temperature susceptibility and hysteresis of magnetite. Earth Planet. Sci. Lett. 169, 51–58.

Nesbitt, H.W., 1979. Mobility and fractionation of rare earth elements during weathering of a granodiorite. Nature 279, 206–210.

Nia, R., 1968. Geologische und petrographische Untersuchungen zum Problem der Boehmit-Diaspor-Genese in griechischen Oberkreide-Bauxiten der Parnass-Kiona-Zone. Unpublished PhD Thesis. University of Hamburg, Hamburg, Germany (133pp).

Nicolas, J., Bildgen, P., 1979. Relations between the location of the karst bauxites in the northern hemisphere, the global tectonics and the climatic variations during geological time. Palaeogeogr. Palaeoclimatol. Palaeoecol. 28, 205–239.

Özdemir, Ö., 1987. Inversion of titanomaghemites. Phys. Earth Planet. Inter. 46, 184–196.

Özdemir, Ö., Banerjee, S.K., 1984. High-temperature stability of maghemite (γ-Fe_2O_3). Geophys. Res. Lett. 11, 161–164.

Özlü, N., 1983. Trace-element content of "karst bauxites" and their parent rocks in the Mediterranean belt. Mineral. Deposita 18, 469–476.

Öztürk, H., Hein, J.R., Hanilçi, N., 2002. Genesis of the Doğankuzu and Mortaş bauxite deposits, Taurides, Turkey: separation of Al, Fe, and Mn and implications for passive margin metallogeny. Econ. Geol. 97, 1063–1077.

Pačevski, A., Moritz, R., Kouzmanov, K., Marquardt, K., Živković, P., Cvetković, L., 2012. Texture and composition of Pb-bearing pyrite from the Čoka Marin polymetallic deposit, Serbia, controlled by nanoscale inclusions. Can. Mineral. 50, 1–20.

Palenik, C.S., Utsunomiya, S., Reich, M., Kesler, S.E., Wang, L., Ewing, R.C., 2004. "Invisible" gold revealed: direct imaging of gold nanoparticles in a Carlin-type deposit. Am. Mineral. 89, 1359–1366.

Plathe, K.L., Von der Kammer, F., Hasellöv, M., Moore, J., Murayama, M., Hofmann, T., Hochella Jr., M.F., 2010. Using FIFFF and a TEM to determine trace metal-nanoparticle associations in riverbed sediment. Environ. Chem. 7, 82–93.

Pohl, W.L., 2011. Economic Geology Principles and Practice: Metals, Minerals, Coal and Hydrocarbons – Introduction to Formation and Sustainable Exploitation of Mineral Deposits. Wiley-Blackwell, Oxford (663 pp.).

Radtke, G., Lazar, S., Botton, G.A., 2006. High-resolution EELS investigation of the electronic structure of ilmenites. Phys. Rev. B 74 (155117), 1–8.

Raj, D., Harchand, K.S., Maini, V., 1993. Characterization of iron minerals in bauxite. Nucl. Inst. Methods Phys. Res. B 76, 242–243.

Ravel, B., Newville, M., 2005. ATHENA, ARTEMIS, HEPHAESTUS: data analysis for X-ray absorption spectroscopy using IFEFFIT. J. Synchrotron Radiat. 12, 537–541.

Readman, P., O'Reilly, W., 1970. The synthesis and inversion of non-stoichiometric titanomagnetites. Phys. Earth Planet. Inter. 4, 121–128.

Reich, M., Utsunomiya, S., Kesler, S.E., Wang, L., Ewing, R.C., Becker, U., 2006. Thermal behavior in metal nanoparticles in geologic materials. Geology 34, 1033–1036.

Reich, M., Hough, R.M., Deditius, A., Utsunomiya, S., Ciobanu, C.L., Cook, N.J., 2011. Nanogeoscience in ore systems research: principles, methods, and applications. Introduction and preface to the special issue. Ore Geol. Rev. 42, 1–5.

Reich, M., Deditius, A., Chryssoulis, S., Li, J.-W., Ma, C.-Q., Parada, M.A., Barra, F., Mittermayr, F., 2013. Pyrite as a record of hydrothermal fluid evolution in a porphyry copper system: a SIMS/EMPA trace element study. Geochim. Cosmochim. Acta 104, 42–62.

Rivas-Sánchez, M.L., Alva-Valdivia, L.M., Arenas-Alatorre, J., Urrutia-Fucugauchi, J., Perrin, M., Goguitchaichvili, A., Ruiz-Sandoval, M., Ramos Molina, M.A., 2009. Natural magnetite nanoparticles from an iron-ore deposit: size dependence on magnetic properties. Earth Planets Space 61, 151–160.

Robb, L., 2005. Introduction to Ore-Forming Processes. Wiley-Blackwell (former Blackwell Publishing), Malden, USA (384 pp.).

Rodríguez-Carvajal, J., 1993. Recent advances in magnetic structure determination neutron powder diffraction. Physica B 192, 55–69.

Royer, D.L., 2006. CO_2-forced climate thresholds during the Phanerozoic. Geochim. Cosmochim. Acta 70, 5665–5675.

Schindler, M., Hochella Jr., M.F., 2016. Nanomineralogy as a new dimension in understanding elusive geochemical processes in soils: the case of low-solubility-index elements. Geology 44 (7), 1–4, G37774.1.

Shoval, S., Gaft, M., Panczer, G., 2003. Luminescence of Cr^{3+} in natural and calcined diaspore. J. Therm. Anal. Calorim. 71, 699–706.

Skelton, P.W., Spicer, R.A., Kelley, S.P., Gilmour, I., 2006. The Cretaceous World. Cambridge University Press, Cambridge, UK (360 pp.).

Smith, S.J., Stevens, R., Liu, S., Li, G., Navrotsky, A., Boerio-Goates, J., Woodfield, B.F., 2009. Heat capacities and thermodynamic functions of TiO_2 anatase and rutile: analysis of phase stability. Am. Mineral. 94, 236–243.

Steuber, T., Rauch, M., Masse, J.-P., Graaf, J., Malkoč, M., 2005. Low-latitude seasonality of Cretaceous temperatures in warm and cold episodes. Nature 437, 1341–1344.

Tauxe, L., 1998. Paleomagnetic Principles and Practice. Springer, The Netherlands (301 pp.).

Tsirambides, A., Filippidis, A., 2012a. Greece seeks mineral lifeboat. Ind. Miner. 2012, 38–45 (January).

Tsirambides, A., Filippidis, A., 2012b. Metallic mineral resources of Greece. Cen. Eur. J. Geosci. 4, 641–650.

Valeton, I., 1972. Bauxites. Elsevier, Amsterdam (226 pp.).

Valeton, I., 1994. Element concentration and formation of ore deposits by weathering. Catena 21, 99–129.

Valeton, I., Biermann, M., Reche, R., Rosenberg, F., 1987. Genesis of nickel laterites and bauxites in Greece during the Jurassic and the Cretaceous and their relation to ultrabasic rocks. Ore Geol. Rev. 2, 359–404.

Verwey, E.J.W., 1939. Electronic conduction of magnetite (Fe_3O_4) and its transition point at low temperatures. Nature 144, 327–328.

Waychunas, G.A., Zhang, H., 2008. Structure, chemistry, and properties of mineral nanoparticles. Elements 4, 381–387.

Wirth, R., Reid, D., Schreiber, A., 2013. Nanometer-sized platinum-group minerals (PGM) in base metal sulfides: new evidence for an orthomagmatic origin of the Merensky reef PGE ore deposit, Bushveld complex, South Africa. Can. Mineral. 51, 143–155.

Zack, T., Von Eynatten, H., Kronz, A., 2004. Rutile geochemistry and its potential use in quantitative provenance studies. Sediment. Geol. 171, 37–58.

Zhou, Y., Fichthorn, K.A., 2012. Microscopic view of nucleation in the anatase-to-rutile transformation. J. Phys. Chem. C 116, 8314–8321.